DARK MATTER DIRECT DETECTION WITH HVeV DETECTOR

By

HUANBO SUN

A DISSERTATION PRESENTED TO THE GRADUATE SCHOOL
OF THE UNIVERSITY OF FLORIDA IN PARTIAL FULFILLMENT
OF THE REQUIREMENTS FOR THE DEGREE OF
DOCTOR OF PHILOSOPHY

UNIVERSITY OF FLORIDA

2025

To my beloved grandfather

ACKNOWLEDGEMENTS

First and foremost, I would like to thank my father. You are the beginning of everything; I could not have started this long journey without your support. You have always given me unwavering understanding and encouragement, even though you never say it.

I am deeply grateful to Prof. Saab for giving me the opportunity to be part of this fascinating work. Thank you for these many years — even when I hesitated or slacked off, you always offered me your full understanding and support.

I would like to thank Valentina and Corey for helping me during the early stage of my research. Your patience and guidance enabled me to quickly gain an understanding of the field. I also want to thank Ziqing, Tom, Lauren, Mat, and all the other collaborators for their kind support and companionship throughout this journey.

I would like to thank Prof. Segre, whose care and support helped me quickly adapt to a new life. Your kindness eased my anxiety and fear during my early days in a foreign country.

I am especially thankful to my girlfriend, Huanxi. You made this lonely journey not lonely, and your companionship gave me the strength and encouragement to keep moving forward.

I would also like to thank Suyang and Yuan. You were the ones I always turned to for help. I truly appreciate all your care and support over the past six years, and I wish you both all the best in the final stage of your PhD.

I would also like to thank my family and relatives. Without your support and help, I could not have come this far.

Lastly, I want to say to my grandfather: I miss you. You gave me endless love and patience, and you have always held the deepest place in my heart. I have now become a scientist — just as I once proudly told you I would. It has been fourteen years since you left, but I still miss you very, very much.

TABLE OF CONTENTS

LIST OF FIGURES

Figures page

LIST OF ABBREVIATIONS

CMB	Cosmic Microwave Background
CT	Charge Trapping
DM	Dark Matter
HV	High Voltage
HVeV	High-Voltage eV-resolution
II	Impact Ionization
iZIP	interleaved Z-sensitive Ionization and Phonon detector
LDM	Light Dark Matter
NEXUS	Northwestern EXperimental Underground Site
QET	Quasiparticle-trap-assisted Electrothermal-feedback Transition-edge sensor
SHM	Standard Halo Model
SQUID	Superconducting Quantum Interference Device
SuperCDMS	Super Cryogenic Dark Matter Search
TES	Transition-Edge Sensor
WIMP	Weakly Interacting Massive Particle

Abstract of Dissertation Presented to the Graduate School
of the University of Florida in Partial Fulfillment of the
Requirements for the Degree of Doctor of Philosophy

DARK MATTER DIRECT DETECTION WITH HVeV DETECTOR

By

Huanbo Sun

May 2025

Chair: Tarek Saab
Major: Physics

This dissertation summarizes my research conducted within the SuperCDMS collaboration, with a particular focus on the HVeV experiment operated at the NEXUS facility.

In Chapter 1, I discuss the background and motivation for dark matter research. Chapter 2 provides an overview of current dark matter detection experiments. From Chapter 3 onward, the focus shifts to the SuperCDMS HVeV experiment. In Chapter 3, I describe the underlying physics principles of the HVeV detector. Chapter 4 introduces the signal model, which characterizes the relationship between dark matter interactions in the detector and the corresponding detector response. In Chapter 5, I discuss background events, including environmental backgrounds and detector-related effects. Finally, in Chapter 6, I present the science run—HVeV Run 4, which represents the latest light dark matter limit obtained by the SuperCDMS collaboration.

A significant focus of this work is the investigation of electron delay release, which is examined in detail in Chapter 5. This phenomenon was first identified due to its exceptionally high event rate and is currently hypothesized to be a detector effect caused by exposure to high-energy external particles. This topic has been one of my major research contributions over the past several years.

CHAPTER 1
DARK MATTER

1.1 Dark Matter Early History

As early as ancient Greece, philosophers began contemplating the possibility of the existence of unobservable matter. With the establishment of physics as a discipline, astronomers started to notice gravitational anomalies among visible stars, leading to the suspicion that unseen celestial bodies might exist. By the 19th century, scientists speculated that invisible stars, gases, and clouds could reside in the dark regions of stellar fields [10]. These phenomena represented early concepts of dark matter, which were later resolved with advancements in technology and observational methods. These accounts illustrate that the concept of invisible or unobservable matter has remained a persistent theme throughout the evolution of physics and cosmology.

As the 20th century approached, the estimation of stellar mass played a crucial role in shaping the modern concept of dark matter. Lord Kelvin proposed a quantitative method to estimate the mass of stars in the Milky Way, while Henri Poincaré was the first to introduce the term "dark matter". Jacobus Kapteyn developed one of the earliest quantitative models for the shape and size of the Galaxy, and Jan Oort derived the upper limit for nebulous or meteoric matter near the Sun [10]. Although the concept of dark matter remained vague at the time, the pioneering work of these scientists laid the foundation for modern dark matter research.

Swiss astronomer Fritz Zwicky is one of the most renowned pioneers in the field of dark matter. He applied the virial theorem to galaxies within the Coma Cluster and famously concluded, "*If this would be confirmed, we would get the surprising result that dark matter is present in much greater amount than luminous matter.*" Based on his groundbreaking work, a key piece of evidence supporting the existence of dark matter gained widespread acceptance.

1.2 Modern Evidence

Dark matter has emerged as one of the greatest mysteries in modern cosmology. Efforts directly to detect dark matter particles have spanned several decades, often leading to disappointing results for scientists. However, evidence supporting the existence of dark matter has grown increasingly compelling. This evidence spans a wide range of scales, from the scale of galaxies to galaxy clusters and even the vast filaments and voids of the cosmic web. Observational results across these scales consistently align with theoretical predictions only when the existence of dark matter is assumed.

1.2.1 Galaxy Rotation Curve

The study of spiral galaxy rotation curves provides clear evidence for the need for additional mass beyond the observable matter on the galactic scale. It reveals a discrepancy between the star rotation velocities predicted by Newtonian mechanics and those measured using the Doppler effect. To reconcile this discrepancy, the presence of dark matter must be introduced.

Based on Newtonian mechanics, assuming the mass distribution within the galaxy is spherically symmetric, the enclosed mass $M_{sph.}(R)$ within a distance R from the galaxy center depends only on the radius length R. For a star in circular motion, its rotation velocity can be predicted using Newtonian mechanics as follows:

$$v_{New.} = \sqrt{\frac{G \cdot M_{sph.}(R)}{R}} \tag{1-1}$$

For general mass distributions, without assuming spherical symmetry, although the calculations become more complex, the rotation velocity can still be predicted if the form of the mass distribution is provided.

At the same time, if the orbit of a circularly moving star is inclined at an angle α relative to the line of sight of the observer, the velocity's projection along the line of sight ($v_{l.o.s.}$) can be measured using the Doppler effect. This is achieved by analyzing the visible light near the galaxy center and the 21 cm hydrogen line in the outer regions of the galaxy. The actual rotation velocity is then given by:

$$v_{Doop.} = \frac{v_{l.o.s.}}{\cos\alpha} \tag{1-2}$$

The galaxy rotation curve is a plot that shows the rotation velocity of stars as a function of their distance R from the galaxy center. A discrepancy arises when comparing the rotation curve predicted by Newtonian mechanics with the rotation curve measured using the Doppler effect. As shown in Figure 1-1. These two velocities follow distinctly different patterns. The rotation velocities increase rapidly with distance R near the galaxy center, primarily because most of the galaxy's mass is concentrated in its central region, causing the total enclosed mass to rise quickly with distance. However, at larger distances, the increase in enclosed mass becomes negligible, and according to Newtonian mechanics, the rotation velocity should decrease as $\frac{1}{\sqrt{R}}$. In contrast to this prediction, the observed rotation velocity remains relatively constant at larger distances, forming a flat curve instead of a declining one.

Scientists attempted to resolve the discrepancy by modifying the mass distribution model to reproduce the observed rotation curve. This approach works well for the visible regions near the galaxy center, where the mass can be attributed to observed luminous matter. However, in the outer regions of the galaxy, where insufficient visible matter exists, there is no way to account for the additional mass required to match the observed velocities.

The only viable solution is to assume the presence of invisible matter. With this assumption, there is no need to alter the visible mass distribution. To match the observed galaxy rotation curve, the total enclosed dark matter mass is expected to be proportional to the distance, expressed as $M_{DM}(R) \propto R$.

1.2.2 Bullet Cluster

The famous Bullet Cluster (1E 0657-56), shown in Figure 1-2, exhibits a phenomenon on the cluster scale that provides strong evidence for the existence of dark matter. At the same time, it presents a significant challenge to alternative theories of dark matter. In this image, the separation between invisible mass and baryonic matter is clearly demonstrated.

The Bullet Cluster was formed through a direct, head-on collision between two sub-clusters. Its major components—galaxies, gas, and dark matter—have been studied using various observational techniques. The galaxies in the cluster, which can be directly observed through visible light, were imaged by the Magellan telescopes and the Hubble Space Telescope, and are

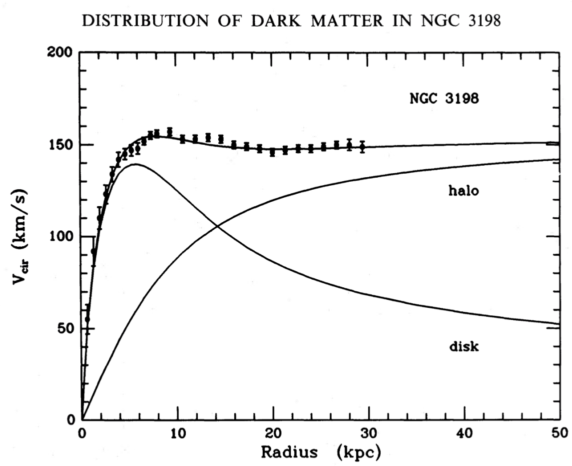

Figure 1-1. The observed galaxy rotation curve data (represented by dots with error bars) and the corresponding fit are shown. The fit is composed of contributions from baryonic matter (disk) and dark matter (halo), demonstrating their consistency with the observed data. Credit: T. S. van Albada et al. [33].

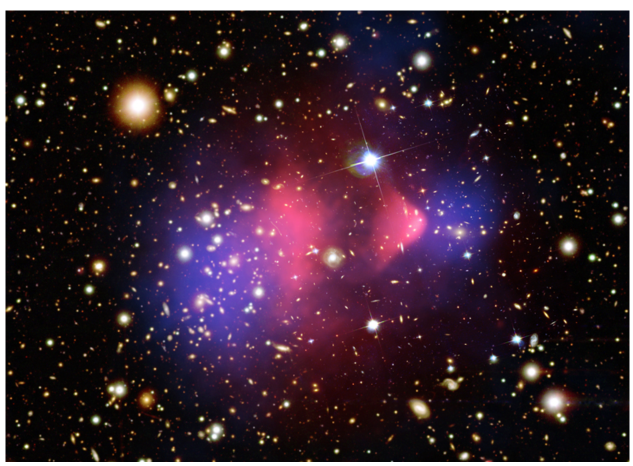

Figure 1-2. The image of the Bullet Cluster clearly illustrates the separation between invisible mass and normal matter. The red region represents the gas, the galaxies are depicted in white and orange, while the blue regions correspond to the invisible mass, detected using gravitational lensing effects. Credit: X-ray: NASA/CXC/CfA/M.Markevitch et al.; Optical: NASA/STScI; Magellan/U.Arizona/D.Clowe et al.; Lensing Map: NASA/STScI; ESO WFI; Magellan/U.Arizona/D.Clowe et al.

depicted in orange and white in the image. The hot gas, on the other hand, was detected using the Chandra X-ray Observatory and is shown as the pink region in the image.

By utilizing the gravitational lensing effect—where light is bent as it passes through massive objects—scientists have identified the most massive regions of the Bullet Cluster, mapped in blue in the image. The study reveals that the majority of the mass is not consistent with the visible matter or galaxies. Such a phenomenon cannot be easily explained without assuming the existence of dark matter. Consequently, the Bullet Cluster image provides strong evidence supporting the existence of dark matter.

1.2.3 Cosmic Web

On the large scale of the observable universe, galaxies are not uniformly distributed but instead form a vast web-like structure known as the cosmic web. Most galaxies are concentrated in filamentary structures, leaving vast voids in between as illustrated in Figure 1-3.

The structure of the cosmic web is shaped by gravity, which pulls matter together to form filamentary structures in some regions while leaving vast voids in others. In other words, the universe exhibits a highly non-linear nature. To understand this non-linear framework, scientists employ N-body simulations to reconstruct the cosmic web and investigate its formation.

However, these simulations reveal that the observed large-scale structures of the current universe cannot be explained solely by Standard Model matter. Observable matter alone cannot generate enough gravitational pull to drive the formation of the non-linear structures we see today within the available cosmic time [26]. Dark matter provides a solution to this challenge. By incorporating additional mass—dark matter particles—into the simulations, scientists have successfully reproduced results that closely align with observable data. Thus, the study of the universe's large-scale structure provides compelling evidence supporting the existence of dark matter on the largest cosmic scales.

1.2.4 CMB

The universe began with the Big Bang, after which it was extremely hot and dense. Matter existed in the form of a plasma composed of protons, electrons, and photons. As the universe

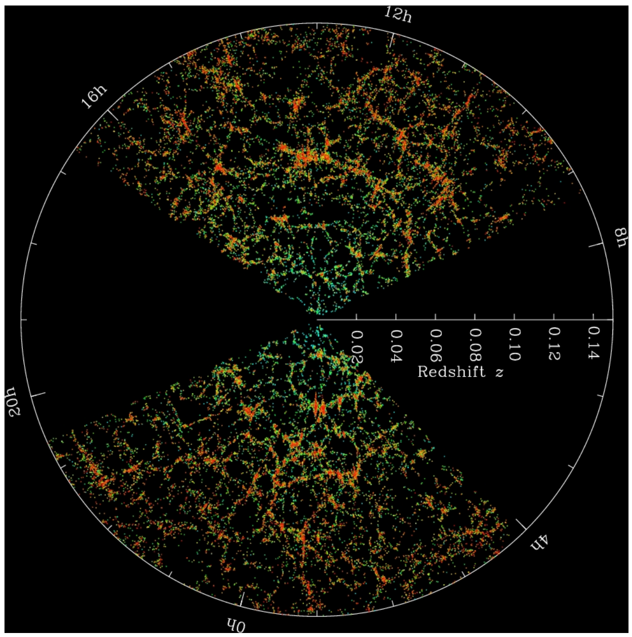

Figure 1-3. A slice of the universe from the Sloan Digital Sky Survey project, where each point represents a galaxy. The figure vividly illustrates the filamentary structures and voids that characterize the cosmic web. Earth is positioned at the center, with redshift z serving as a measure of distance from this central point. The outermost circle represents a distance of approximately 2 billion light-years from Earth. The angle is measured with Right Ascension, expressed in units of hours. Credit: M. Blanton and Sloan Digital Sky Survey

expanded and cooled, it reached a critical point around 380,000 years after the Big Bang, when photons decoupled from the dense plasma — a period known as the recombination epoch. At this stage, the universe became transparent, allowing photons to propagate freely. These photons represent the first light of the universe and carry valuable information about its state at that time.

As the universe continued to expand, these first photons experienced redshift. However, they continued to propagate freely through space and can still be detected today using high-resolution microwave detectors. The photons that originated during the recombination epoch and have traveled through the universe unimpeded until the present day are known as the cosmic microwave background (CMB). Figure 1-4 is the CMB temperature map, presenting observational data from the Planck satellite. It reveals the matter density distribution in the early universe. The CMB temperature map reveals the overall uniform matter density of the universe. However, it still exhibits small density fluctuations, highlighted by the different colors in the map. These tiny variations in density served as the initial seeds for cosmic structure formation, eventually evolving into the nonlinear structures of the universe, such as galaxies, galaxy clusters, and other large-scale formations.

Further analysis of the CMB temperature map via spherical harmonic decomposition reveals its angular power spectrum across different scales. A widely accepted model in modern cosmology is the Lambda cold dark matter model (ΛCDM model). The ΛCDM model provides an excellent fit to the observed power spectrum of the CMB, but only when the existence of dark matter is included. Moreover, this model predicts that dark matter constitutes approximately 26% of the total mass-energy of the universe, aligning with observational data from Planck and other cosmological surveys.

1.3 General Dark Matter Background

Based on cosmological studies, the universe is composed of dark energy, dark matter, and ordinary matter (often referred to as baryons). Among these components, dark energy accounts for approximately 70% of the total mass-energy content, dark matter contributes about 26%, while ordinary matter makes up only 4%.

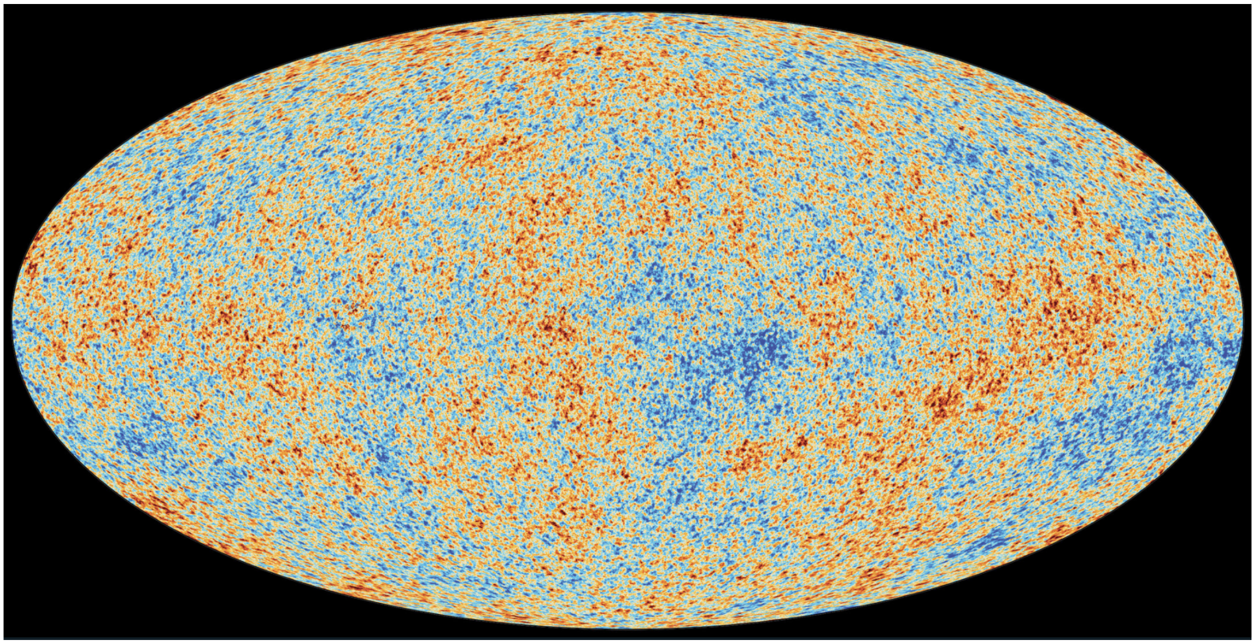

Figure 1-4. The cosmic microwave background (CMB) consists of photons that decoupled from the dense plasma of protons, electrons, and photons when the universe was about 380,000 years old. It represents the first light of the universe, providing a snapshot of its early state. Credit: ESA/Planck Collaboration.

Furthermore, without delving into specific models, dark matter is expected to exhibit some general, model-independent properties. First and foremost, dark matter should be ”dark”—meaning it does not carry electric charge and therefore does not interact electromagnetically, or at least not in any significant way. Secondly, dark matter particles interact gravitationally, which is the primary clue that led to their discovery. Thirdly, dark matter is stable, with a lifetime exceeding the age of the universe. It is believed to have been produced in the early universe when energy densities were extremely high. As the universe expanded and cooled, the production of dark matter effectively ceased. Therefore, dark matter particles must remain stable to account for the current relic density observed today. Finally, dark matter is considered collisionless, meaning it can only have a tiny scattering cross-section with ordinary matter. As observed in the case of the Bullet Cluster , dark matter and ordinary matter effectively separate during collisions. If dark matter had a relatively larger scattering cross-section, this separation effect would be significantly altered. For more details about dark matter theory, readers can refer to the paper [26].

There are various dark matter models proposed, covering a wide range of energy scales—from zeV to masses exceeding that of the Sun. Figure 1-5 highlights some of the prominent dark matter candidates across different energy ranges. Among these candidates, Weakly Interacting Massive Particles (WIMPs) and sub-GeV-scale dark matter, are of particular interest to the SuperCDMS collaboration. These will be discussed in greater detail in the following Section 1.3.1 and Section 1.3.2.

1.3.1 WIMPs

Weakly Interacting Massive Particles (WIMPs) are a particular dark matter model which of mass around GeV to TeV. Its the most popular dark matter model, attracting the attention of the whole physics community over several decades. In addition to the general properties of dark matter, WIMPs are assumed to be cold—non-relativistic massive particles. They are also capable of scattering off ordinary matter with an interaction strength comparable to the weak force.

In supersymmetry (SUSY) theories, every known particle has a counterpart particle with a different spin. Furthermore, SUSY naturally predicts the existence of WIMPs as dark matter candidates. The abundance of WIMPs in the modern universe can be explained by the freeze-out mechanism. In the early universe, energy density and particle density were extremely high, and particles interacted frequently, maintaining thermal equilibrium. The production and annihilation rates of particles were balanced during this phase. As the universe expanded and cooled, the particle density decreased, causing the annihilation rate to drop significantly. At a certain point, the annihilation rate became too low to maintain equilibrium, and the particle species ”froze out,” leaving behind a relic density of particles. Remarkably, the relic density of dark matter aligns with the predicted density of WIMPs, a phenomenon referred to as the ”WIMP miracle.”

1.3.2 LDMs

Even though WIMPs are a natural prediction that aligns with many theories and observations, their detection has yet to yield positive results. The sensitivity of experimental

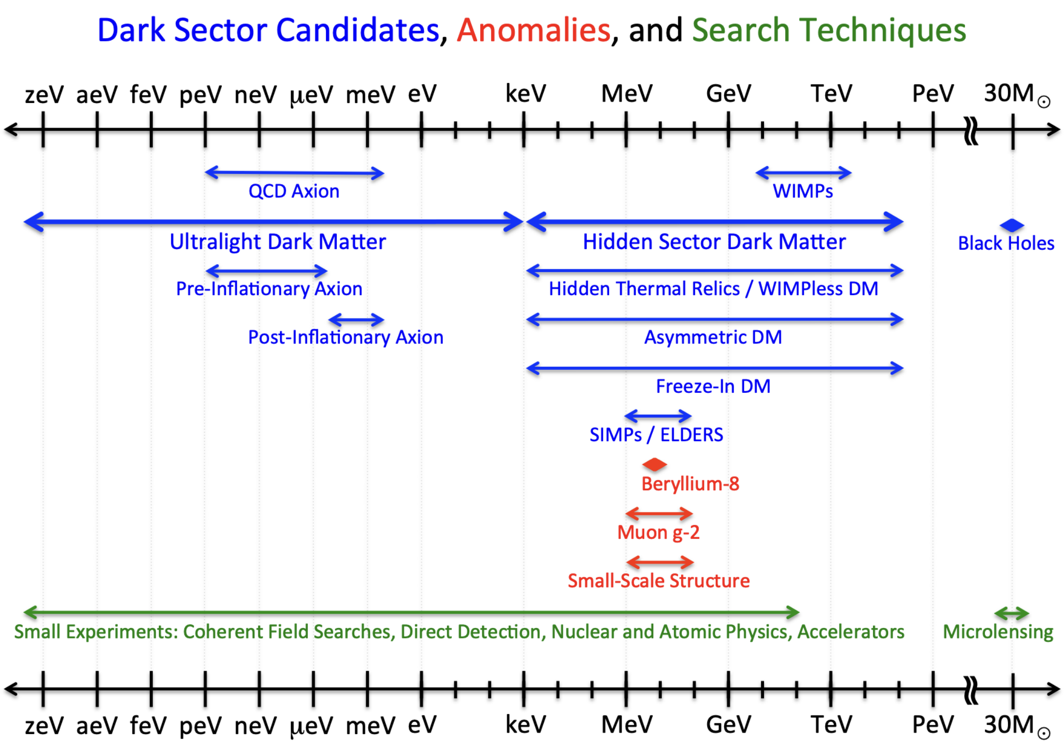

Figure 1-5. An overview of representative dark matter particle candidates across different mass ranges is shown in blue. The green labels at the bottom indicate the experimental technologies used to explore dark matter candidates within each specific range. The observed experimental anomalies (as of 2017), highlighted in red, may suggest the need for new physics. Credit: [8].

detectors searching for WIMPs is now approaching the neutrino background, leaving little room for further improvement. Consequently, the parameter space for WIMPs is becoming increasingly constrained. Furthermore, the Large Hadron Collider (LHC) has reached the energy scales required to produce particles predicted by the simplest supersymmetry (SUSY) models, yet no signs of new particles have been observed. These developments have diminished confidence in the WIMP hypothesis as the primary explanation for dark matter.

With advancements in technology, researchers have increasingly focused on the sub-GeV mass scale. Dark matter particles with masses within this range are collectively referred to as light dark matter (LDM). LDM is not a specific dark matter model but rather a general classification encompassing all possible dark matter particles with sub-GeV masses. LDM is a key focus of the SuperCDMS HVeV program, which aims to search for both scattering and absorption interactions of LDM. For more details, please refer to Section 4.1.

CHAPTER 2
DARK MATTER EXPERIMENTS

2.1 Dark Matter Direct Searching Methods

Various astrophysical observations and studies suggest that dark matter may weakly interact with Standard Model particles. Many experiments leverage this property to detect dark matter by tracking the signals generated from its interactions with baryonic matter. These detection methods are collectively referred to as dark matter direct detection methods.

The energy transfer efficiency between dark matter particles and the detection target strongly depends on the comparability of their respective masses. For GeV-scale dark matter particles (WIMPs), nuclei are the optimal targets for energy transfer efficiency due to their similar mass. In contrast, for sub-GeV-scale dark matter particles (LDMs), electrons in the target material become the preferred interaction candidates.

Most dark matter direct detection experiments are designed to utilize nuclear recoil signals to search for WIMPs. In these experiments, electron recoil is typically classified as background, making it critical to reject events originating from electron recoils. However, the sensitivity of current GeV-scale dark matter experiments is approaching the neutrino floor, which is discussed in Section 5.1.2, and the search for dark matter has so far yielded null results. To address these limitations, new technologies and advanced analysis methods are being employed to either enhance existing experiments or develop new ones, focusing on the exploration of LDMs through electron recoil. Consequently, the ability to effectively reject non-dark matter electron recoil events becomes critically important.

2.1.1 Noble Liquids Experiments

Liquid xenon and liquid argon are commonly used as target materials in dark matter direct detection experiments. When dark matter particles scatter within the target, both scintillation and ionization occur. These signals can be utilized to extract valuable information about the interaction. Liquid xenon detectors are capable of achieving a lower energy threshold [22], making them more sensitive to low-energy range of dark matter interactions. In liquid argon detectors, the difference in the scintillation pulse shape between nuclear recoils and electron recoils provides an effective means of discrimination [12].

2.1.1.1 Dual-Phase Liquid Xenon Experiments

Experiments utilizing dual-phase liquid xenon detectors currently set the strongest constraints on GeV-scale dark matter. Notable examples include the LZ experiment at SURF, PandaX-4T at CJPL, and XENONnT at LNGS [12, 22]. A typical dual-phase liquid xenon detector is shown in Figure 2-1. When a dark matter particle scatters off either xenon nuclei or xenon electrons, scintillation occurs at the interaction site. The scintillation light is detected by photomultiplier tubes (PMTs) and recorded as the S1 signal. In addition to scintillation, electrons are ionized at the interaction site. By applying drift and extraction electric fields within the detector, these electrons are transported from the liquid xenon into the gaseous xenon phase, where they generate electroluminescence. The photons produced during this process are also collected by PMTs and recorded as the S2 signal [6, 22].

By analyzing S1 and S2 signals, researchers can reconstruct various useful pieces of information. The x and y positions of the interaction can be directly determined from the PMTs readings, while the z position can be reconstructed by calculating the time difference between the S1 and S2 signals. Additionally, the ratio between the strengths of S1 and S2 allows researchers to discriminate between nuclear recoil events from electron recoil events backgrounds [6].

Besides exploring WIMPs through the combined analysis of S1 and S2 signals, fully abandoning the S1 signal and performing an S2-only search can extend the capabilities of these detectors to explore LDMs. At such low nuclear recoil energies, the primary scintillation signal is typically absent [5], prompting researchers to rely solely on the electroluminescence signal generated by ionized charges. This approach reduces the detection energy threshold to approximately 1 keV [5].

2.1.1.2 Single-Phase Liquid Argon Experiment

The DEAP-3600 experiment at SNOLAB utilizes a single-phase liquid argon detector to search for WIMPs. The detector contains approximately 3296 kg of liquid argon within a 1.7 m

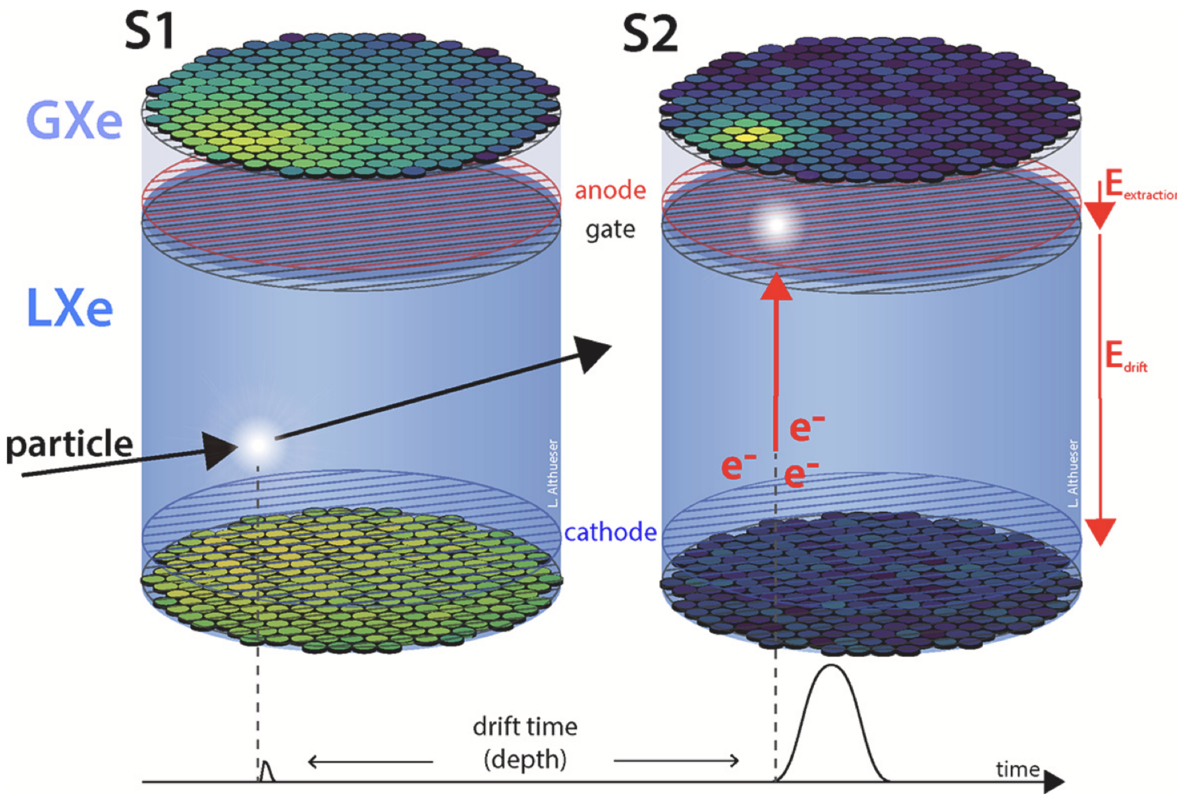

Figure 2-1. This figure illustrates the working principle of the dual-phase XENON detector. When a particle interacts within the detector (left), it deposits energy, generating primary scintillation photons and ionization electrons. These primary photons are detected by the PMTs at the top and bottom of the detector and recorded as the S1 signal. The ionization electrons drift upward under an electric field and are extracted into the gas phase, where electroluminescence photons are generated and recorded by the PMTs as the S2 signal. The time difference between the S1 and S2 signals is used to determine the depth of the interaction event. Credit: [6].

diameter acrylic vessel [34]. When WIMPs deposit energy into the liquid argon, the resulting photon signals are detected by photomultiplier tubes (PMTs). Using pulse shape discrimination (PSD), electron recoil background events can be directly rejected based on their characteristic pulse shapes [2].

2.1.2 Superheated Liquid Experiment

A superheated liquid is filled within a bubble chamber. When dark matter particles scatter off the liquid, small bubbles are generated, which are then detected by a camera system [12]. The thermal properties of the liquid, such as its temperature and pressure, can be adjusted, allowing variation in the energy threshold. This tunability enables the system to be sensitive to nuclear recoil events—typical of WIMPs' recoil energy range—while remaining insensitive to electron recoil backgrounds [29].

Superheated liquid detectors widely use ^{19}F (fluorine-19), whose unpaired proton provides spin, making ^{19}F highly sensitive to spin-dependent interactions with dark matter particles. The PICO collaboration has conducted several superheated liquid dark matter experiments of varying sizes and is currently constructing the PICO-500 experiment at SNOLAB. This experiment will use 250 liters of superheated freon C_3F_8 as the target material [22], to further investigate the dark matter parameter space.

2.1.3 Cryogenic Crystal Experiments

When dark matter interacts with a crystal detector, either through nuclei or electrons, it can produce not only phonon signals but also electron-hole pair ionization and scintillation. These properties enable the development of various solid-state detectors, each optimized for specific detection strategies. For instance, the SuperCDMS detectors utilize both the generated phonon signals and ionized electron-hole pairs, allowing the exploration of a wide range of dark matter masses. The SENSEI experiment focuses on precisely detecting ionized electron-hole pairs, achieving sub-electron discrimination. The CRESST experiment employs scintillation as an effective tool for background rejection. In this approach, events that generate ionization and phonon signals accompanied by scintillation are accepted as potential signals, while others are classified as background.

2.1.3.1 SuperCDMS Experiment

The SuperCDMS SNOLAB experiment, focus on searching for WIMPs, currently under construction, employs two types of detectors: the HV detectors, which amplify and convert the ionization signal into a total phonon signal for improved energy resolution, and the iZIP detectors, which measure both charge and phonon signals to distinguish between nuclear recoil and electron recoil events. The SuperCDMS HVeV detectors are similar to the HV detectors but differ in scale and optimization. The HVeV detectors use a gram-scale silicon design, making them particularly well-suited for precise detection of LDM. By applying a high voltage to the crystal, the detector achieves an ultra-low energy threshold and is capable of distinguishing single charges. The details of these detectors are discussed extensively in Chapter 3.

2.1.3.2 SENSEI Experiment

The SENSEI experiment at SNOLAB is currently setting the most stringent limits on Light Dark Matter (LDM). The experiment utilizes a silicon crystal as the dark matter absorber and employs Skipper CCDs (Charge-Coupled Devices) to precisely count the number of charges generated by dark matter interactions [1].

A CCD consists of numerous pixels, each capable of collecting charge. The traditional method reads out the charge in a pixel by draining it into a readout component, during which the charge is consumed. However, Skipper CCD technology introduces a nondestructive readout process, where the charge in a pixel is repeatedly measured without being depleted. This allows for multiple readouts of the same pixel, significantly improving the signal-to-noise ratio and achieving sub-electron readout noise [31].

To reduce dark current, which results from electrons being thermally promoted into the silicon conduction band, the CCD device is cooled to 125–145 K using a cold finger [31, 1]. When dark matter scatters off electrons in silicon atoms, it can ionize electron-hole pairs. By applying a bias voltage across the silicon crystal, electrons are drifted into pixels. The number of electrons within each pixel is then read out multiple times to precisely determine the total count. The total number of events is correlated with the total number of electrons counted, thereby setting limits on LDMs [1].

2.1.4 Directional and Annual Modulation Detectors

Based on simulation results, local dark matter particles are assumed to be distributed within an isotropic and isothermal sphere, with a density profile following $\rho(r) \propto r^{-2}$ and a velocity distribution described by the Maxwell–Boltzmann distribution [22]. This dark matter halo model is commonly referred to as the Standard Halo Model (SHM).

Under the assumption of the SHM, the Sun, along with the Earth, moves toward the Cygnus constellation as it passes through the dark matter halo. This motion of the solar system generates an apparent "dark matter wind" in the opposite direction. The expected direction of the dark matter wind is a key signature that could reveal the existence of dark matter. Due to the complexity of reconstructing the trajectories of electrons, current directional detectors focus on averaging the recoil directions of nuclei, primarily probing WIMPs. At keV-scale nuclear recoil energies, the track length of recoiling nuclei is approximately 1 mm in gases and around 1 μm in solids [12]. As a result, most current experiments, such as the Cygnus and CYGNO experiments, utilize gas-based Time Projection Chambers (TPC).

In addition to the motion of the solar system through the dark matter halo, the Earth's rotation around the Sun induces an annual modulation in the dark matter scattering rate, as described by Equation 2-1.

$$\frac{dR}{dE}(E,t) \approx S_0(E) + S_m(E)\cos\omega(t - t_0)[17] \tag{2-1}$$

Here, the term S_0 represents the average scattering rate, while $S_m(E)$ denotes the amplitude of the modulation term. The angular frequency ω is equal to $\frac{2\pi}{1year}$, and t_0 is the phase factor of the modulation. The total scattering rate $\frac{dR}{dE}(E,t)$ reaches its maximum around June 2 and its minimum around December 2 [9]. By observing the small variations in the total scattering rate $\frac{dR}{dE}(E,t)$, it becomes possible to confirm the existence of dark matter.

The DAMA experiment, in Italy, utilizes NaI crystals as dark matter absorbers, in room temperature. When WIMPs scatter off the NaI crystals, scintillation photons are generated, which are subsequently detected by photomultiplier tubes (PMTs). The DAMA/LIBRA experiment successfully observed annual modulation signals, as shown in Figure 2-2. However, the results are inconsistent with those of several other dark matter experiments, leaving this signal as a significant mystery. The COSINE-100 experiment, located in the Yangyang Underground Laboratory in Korea, is designed to further investigate the DAMA results using the same NaINaI crystal technology. The work of the COSINE-100 experiment is currently ongoing.

2.2 Indirect Detection Method and Production Method

The understanding of dark matter particles is still limited. Therefore, scientists employ a ”wide net” strategy to search for dark matter particles using all possible technological approaches. In addition to directly detecting signals from dark matter particles, indirect clues hidden within Standard Model particles can help scientists deduce the properties of dark matter, providing valuable complementary insights to direct detection experiments.

Indirect detection experiments aim to identify an excess flux of Standard Model particles from the universe, such as electrons, positrons, X-rays, neutrinos, and others, where the observed flux significantly exceeds the expected background levels. These excess particles are hypothesized to be produced by dark matter decay or pair-annihilation processes. By analyzing the information carried by these particles, scientists can infer the properties of dark matter.

The production method, on the other hand, focuses on the possibility that dark matter particles can be generated in high-energy particle colliders during collisions of two particle beams. When dark matter is produced, it carries away a portion of the energy and momentum. Since dark matter particles are not directly observable in such experiments, researchers analyze the states of the initial and final Standard Model particles to identify missing energy or missing momentum. These observations, in turn, provide valuable information about the properties of dark matter particles.

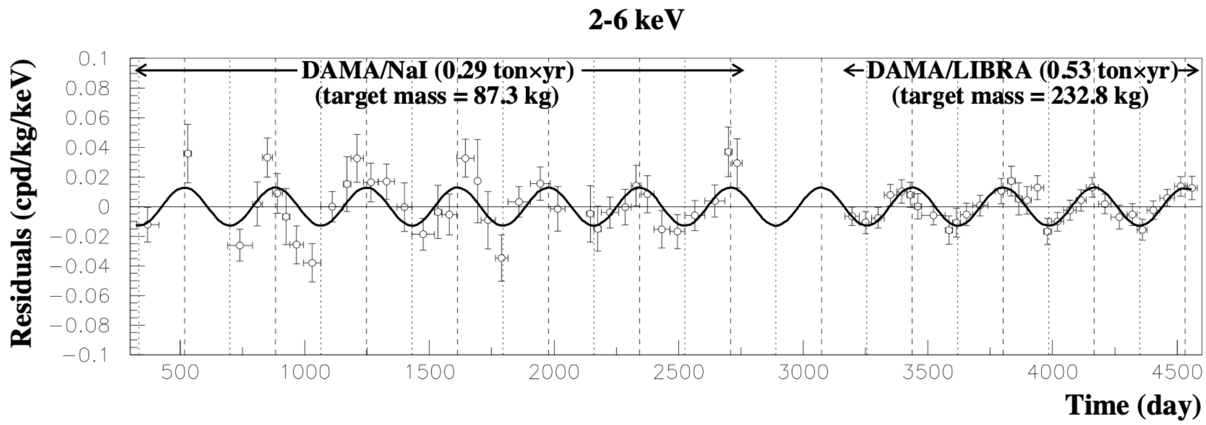

Figure 2-2. The model-independent residual rate in the 2–6 keV energy range, as observed by the DAMA experiment, shows a consistent annual modulation signal. This signal has been consistently observed across multiple data-taking periods over more than ten years. Credit: [9].

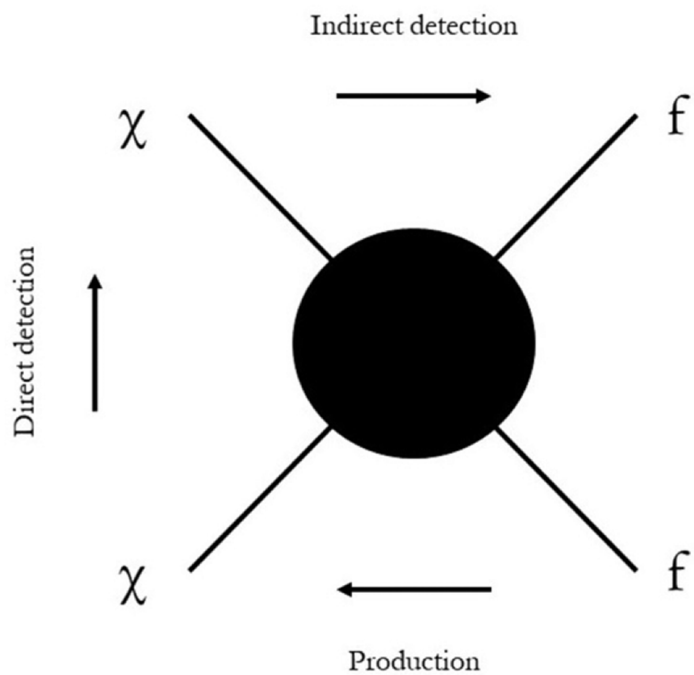

Figure 2-3. Diagram of dark matter interactions and detection methods. χ represents dark matter particles, while f represents Standard Model particles. The arrows indicate the interaction directions. Based on these possible interaction directions, scientists design different detection experiments employing various methods. Credit: [7].

As shown in Figure 2-3, the direct detection method, along with the indirect detection and production methods, complement each other in helping scientists probe the various possibilities of dark matter interactions.

2.3 Recent Direct Detection Limits on Dark Matter

Over the past decade, direct detection experiments have made significant progress in the search for dark matter particles, notably by reducing background levels through various shielding strategies. In addition to the traditional WIMP–nucleon scattering approach, experiments targeting light dark matter (LDM) via electron scattering have been setting increasingly stringent limits.

Figure 2-4 presents the latest upper limits on the spin-independent WIMP–nucleon cross section, while Figure 6-5 shows the most recent constraints from LDM–electron scattering experiments. For exclusion limits on other dark matter models, readers are referred to the official websites of the corresponding experiments.

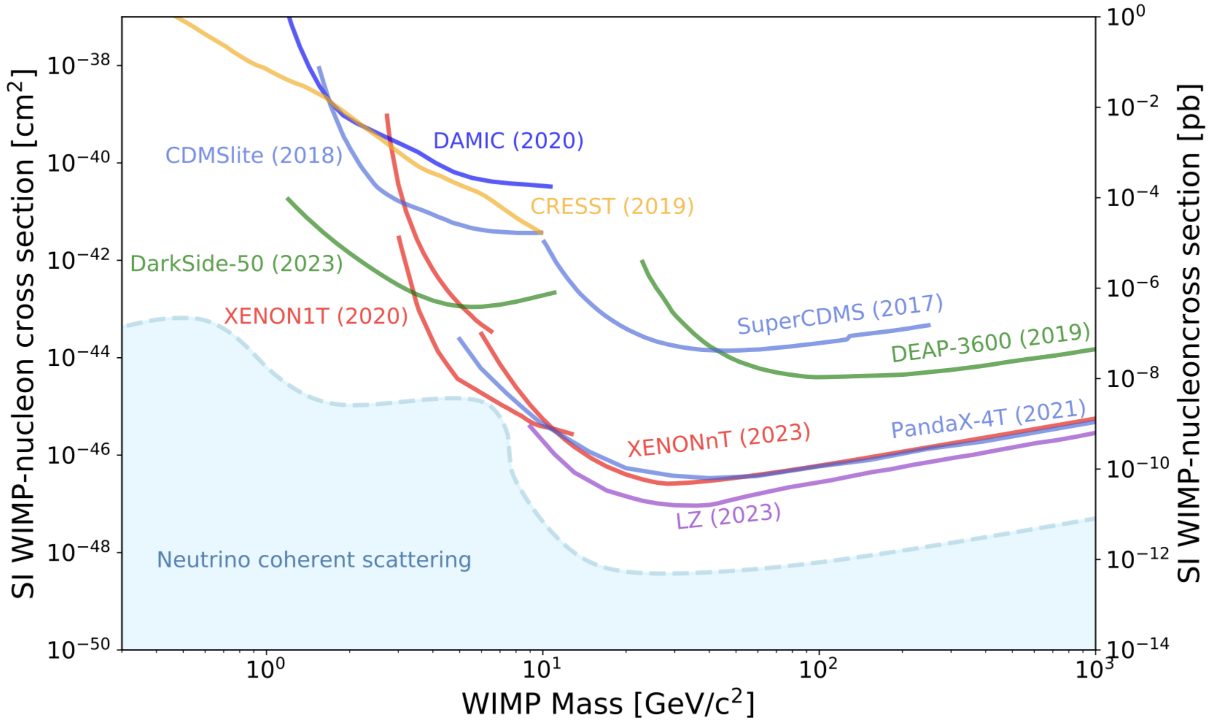

Figure 2-4. The latest upper limits on the spin-independent WIMP–nucleon scattering cross section as a function of WIMP mass, based on results from several major experiments. The shaded blue region at the bottom represents the irreducible background from coherent neutrino scattering, commonly referred to as the “neutrino floor” or “neutrino fog”. Credit: [22].

CHAPTER 3
DETECTOR PHYSICS

3.1 SuperCDMS Detectors

Under the assumption that dark matter can weakly interact with normal matter, as a dark matter particle passes through a crystal, it has the possibility to interact with the crystal, leaving a traceable path and thus making direct detection possible. A dark matter particle can scatter off the crystal's atomic nuclei, depositing energy and momentum to the nuclei and perturbing the electron cloud surrounding them, ionizing the electrons into conduction band. Such electron ionization or excitation is referred to as the Migdal effect. Besides interacting with nuclei, dark matter particles can also scatter off or be absorbed by the atoms' electrons, thus ionizing electrons directly. If an electron is ionized, the crystal yields electron-hole pairs along with phonons. Researchers can relate the number of phonons and electron-hole pairs produced per unit time to the dark matter scattering rate, thereby constraining the properties of the dark matter candidate.

Experiments operated by the SuperCDMS collaboration utilize cryogenic crystal to explore dark matter particles across various models. The SuperCDMS HVeV and HV detectors are designed to measure and amplify the signal produced by electron-hole pairs but lose the ability to distinguish between nuclear recoil and electron recoil events. In contrast, the iZIP detectors are designed to counting the number of produced electron-hole pairs and also measure produced phonons energy but lack the ability to amplify the signal.

3.1.1 SuperCDMS HV and HVeV Detector

SuperCDMS HV and HVeV detectors apply an external high voltage across the top and bottom surfaces of the crystal, as shown in Figure 3-1, where a bias voltage V_{bias} is applied. When dark matter ionizes electrons from the valence band into the conduction band, the crystal produces electron-hole pairs. Due to the applied voltage, the electrons drift toward the higher voltage surface, while the holes drift toward the lower voltage surface. During their transport, the electrons and holes can scatter with the crystal lattice, producing secondary phonons known as Neganov-Trofimov-Luke (NTL) phonons. HV and HVeV detector only have phonon readout system, thus they lost the ability to directly counting the number of electron-hole pairs, however

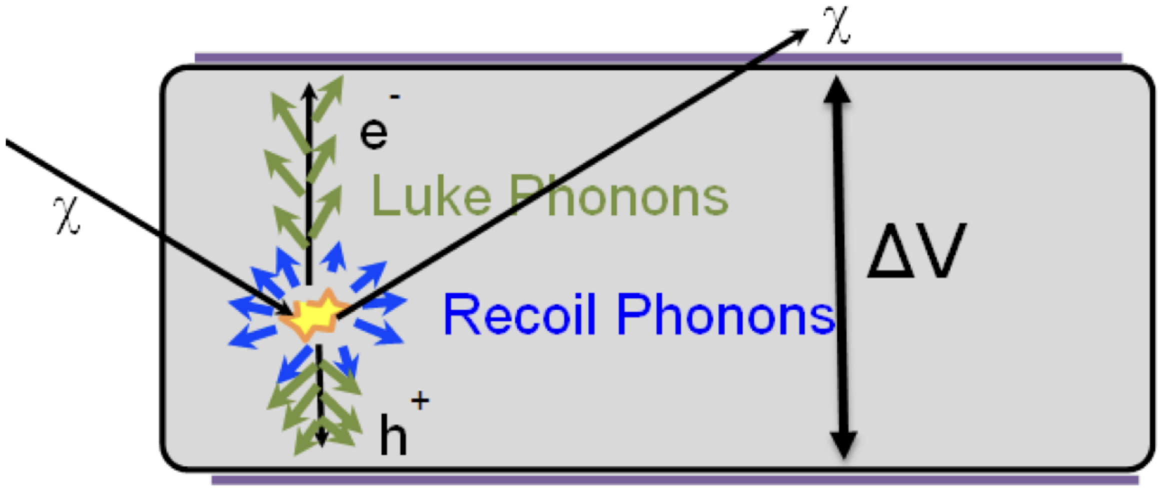

Figure 3-1. A schematic of the dark matter scattering process. In contrast, for the dark matter absorption case, no outgoing dark matter particle is produced. When dark matter interacts with the crystal, it deposits energy, which can ionize electrons into the conduction band and generates primary recoil phonons. These ionized electrons are then drifted under the influence of the bias voltage, and as they move through the crystal lattice, they scatter with crystal lattice and produce additional Luke phonons. This process is referred to as the Neganov–Trofimov–Luke (NTL) effect. Credit: [20]

because of the NTL effect, they achieve the ability to amplify the signals thus reaching to a better charge resolution.

Since every pair of electron and hole together traverse a displacement equal to the thickness of the crystal, the electric potential energy imparted to a electron-hole pair is equal to $e \cdot V_{bias}$ in unit of eV, and these energy are dissipated into the crystal with the form of Luke phonon. The total phonon energy that being measured is thus equal to the primary recoil phonon energy plus the total secondary Luke phonon energy, as is shown in the Equation 4-7 presented below:

$$E_{ph} = E_r + n_{eh} \cdot e \cdot V_{bias} \tag{3-1}$$

Where E_r is the primary recoil phonon energy and n_{eh} is the number of electron-hole pairs being produced at a recoil event.

Because the primary recoil phonon energy E_r is small compared to the Luke phonon energy, HVeV and HV detectors are expected to exhibit a series of quantized peaks, each with an energy that is an integer multiple of $e \cdot V_{bias}$, measured in eV. Figure 3-2 shows data from the HVeV science run conducted in 2021, where the quantized peaks are clearly visible. Besides dark matter particles, photon, beta, gamma, etc. can also ionize the electrons into conduction band, and producing the mimic dark dark matter signal into the final data. These kinds of events are refereed as background event, details of background event are discussed in the chapter ”Background events”.

SuperCDMS HV detectors, shown in Figure 3-3, are made from either silicon or germanium, with a silicon HV detector weighing 0.61 kg and a germanium HV detector weighing 1.39 kg. Silicon and germanium HV detectors are stacked together to form two detector towers, as shown in Figure 3-4. The HV detectors are designed to detect WIMPs - GeV energy scale, and their large mass significantly increases the experiment's exposure. The SuperCDMS HVeV detector, shown in Figure 3-3, on the other hand, is designed to probe sub-GeV dark matter. It is a small silicon detector weighing around 1 gram. Due to its small volume, the energy readout components, TES, can be limited into a small mass and reducing heat capacity, thus the HVeV detector can achieve single-charge resolution.

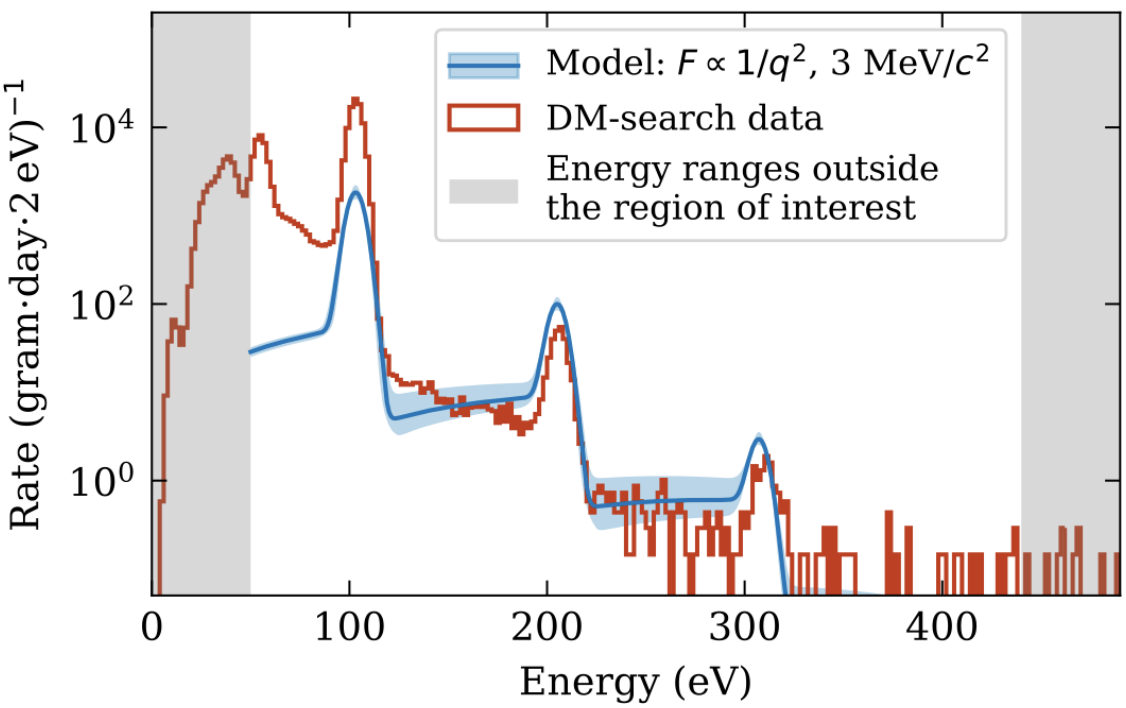

Figure 3-2. An example of HVeV data showing quantized peaks, which correspond to events with different numbers of electron-hole pairs. The red curve represents experimental data from HVeV Run 3 in 2021, after applying data selection criteria. The blue curve illustrates a simulated signal expected from dark matter particles with a form factor of $F \propto \frac{1}{q^2}$ and a mass of 3 MeV/c^2. Credit: [4]

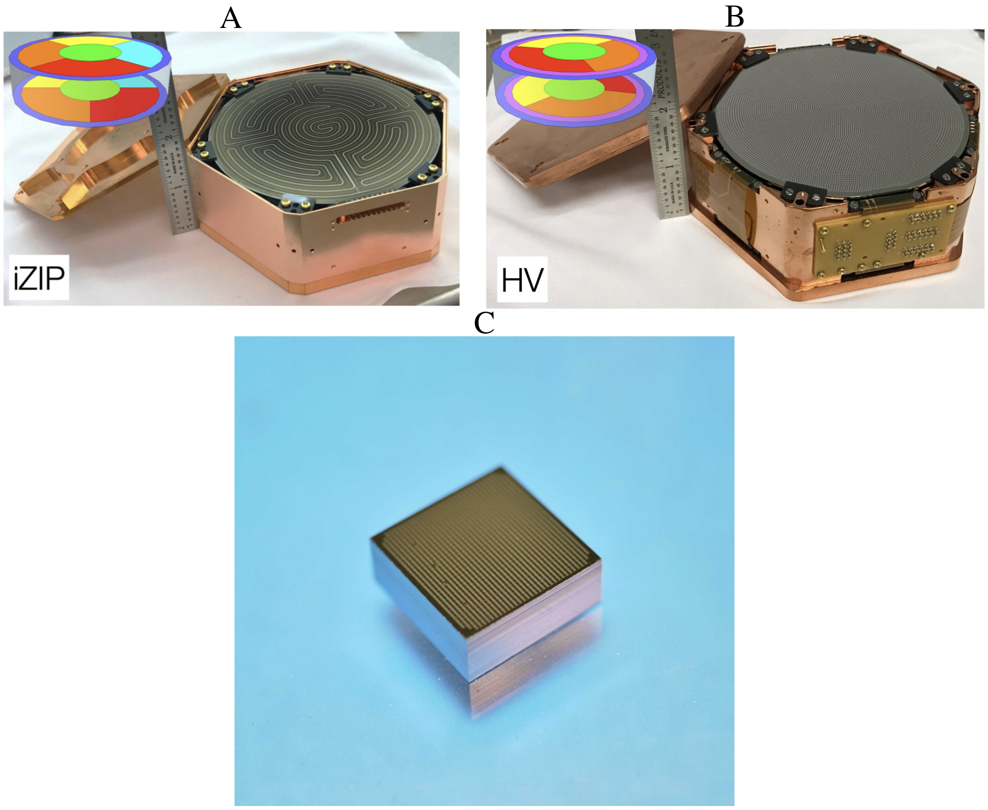

Figure 3-3. Different types of SuperCDMS dark matter detectors. (A) The SuperCDMS iZIP detector, which operates at low voltage to preserve the ability to discriminate between nuclear and electron recoils.(B) The SuperCDMS HV detector, which operates in high-voltage mode to amplify the total signal at the cost of losing nuclear and electron recoil discrimination. (C) The SuperCDMS HVeV detector, a miniaturized version of the HV detector (weighing approximately 1 gram), designed to reduce the total TES mass and achieve single-charge sensitivity. Credit: SuperCDMS collaboration.

3.1.2 SuperCDMS iZIP Detector

SuperCDMS iZIP detectors are similar to HV detectors, with both silicon and germanium versions, and multiple detectors stacked together to increase exposure, as shown in Figures 3-3 and 3-4. Unlike the HV and HVeV detectors, which operate at high bias voltages, iZIP detectors use a lower bias voltage—6V for germanium and 8V for silicon. This low bias voltage serves to drift electron-hole pairs to the surface with minimal amplification, resulting in lower charge resolution in the phonon readout channel. In addition to the phonon readout, the iZIP detectors include a direct charge readout system, which can count the electron-hole pairs produced without relying on the NTL effect, though at the cost of reduced charge resolution.

While both the phonon and charge readout systems in the iZIP have lower charge resolution, the iZIP allows researchers to distinguish between electron and nuclear recoil events by comparing the ratio of electron-hole pairs to primary phonon energy. Electron recoils generally produce more charges than nuclear recoils, making this distinction possible.

3.2 Phonon Signal Readout System

The phonon signal readout is achieved using quasiparticle-trap-assisted electrothermal-feedback transition-edge sensors (QETs). The schematic of the energy flow is shown in Figure 3-5. The device is cooled to around 10 mK to significantly reduce thermal phonon signals, so only phonons from dark matter interactions or from the NTL effect are relevant. When phonons are created within the germanium or silicon crystal substrate, they can enter the superconducting aluminum fin deposited on the substrate, where they break Cooper pairs in the aluminum, creating quasiparticles. An overlap region between the aluminum fin and the tungsten TES serves as a trap for these quasiparticles. Because tungsten has a smaller superconducting energy gap than aluminum, quasiparticles tend to migrate into and become trapped in the overlap region with tungsten. As the quasiparticles become trapped, they release energy by emitting additional phonons, which in turn heat the tungsten TES.

The tungsten TES acts as a thermistor that measures the total heat transferred to it, which can then be used to estimate the total phonon energy generated within the crystal substrate. The tungsten TES is biased in its mid-transition state, as shown in Figure 3-6, where its resistance is highly sensitive to small temperature changes. When the mid-biased tungsten TES absorbs heat, it shifts from the mid-transition state to a normal resistive state. This change in resistance induces a current change in the TES circuit. The tungsten is maintained in a thermal bath, so this resistance change is brief, the thermal bath cools the tungsten back to its mid-transition state, allowing the detector to reset and await the next signal.

A single QET system is designed to be very small, optimizing its performance. To fully capture the phonon energies produced within the detector crystal, multiple QETs are connected in parallel to cover a larger crystal area, ensuring efficient phonon collection. The HVeV detector,

	iZIP		HV	
	Ge	Si	Ge	Si
number of detectors	10	2	8	4
Voltage bias (V)	6	8	100	100

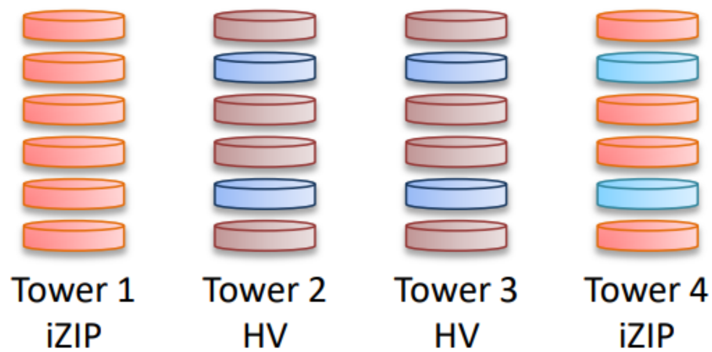

Figure 3-4. Detector towers will be deployed at SNOLAB. By stacking multiple detectors, the total exposure can be significantly increased, thereby enhancing the probability of detecting dark matter interactions. Furthermore, stacking detectors allows researchers to study background coincidences between individual detectors, improving the understanding of background sources. The number of silicon and germanium detectors used in each tower, along with their operational conditions, are shown in the figure. Credit: SuperCDMS collaboration.

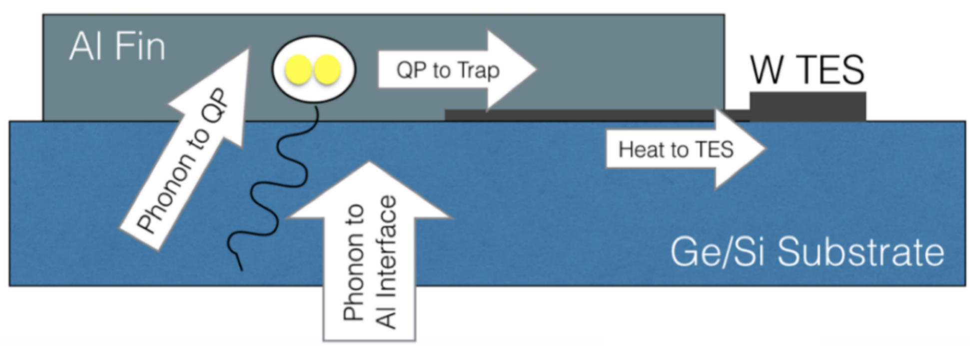

Figure 3-5. A schematic illustrating the energy flow following the deposition of energy by an external particle inside the crystal substrate. Phonons, including primary phonons and secondary Luke phonons, can break Cooper pairs within the superconducting aluminum (Al) fin, generating quasiparticles. Due to the proximity effect between tungsten and aluminum in the trap region, these quasiparticles diffuse toward the trap. Once trapped, the quasiparticles release their energy as heat to the tungsten TES, inducing a resistance change in the tungsten, which is in its mid-transition state. Credit: [20].

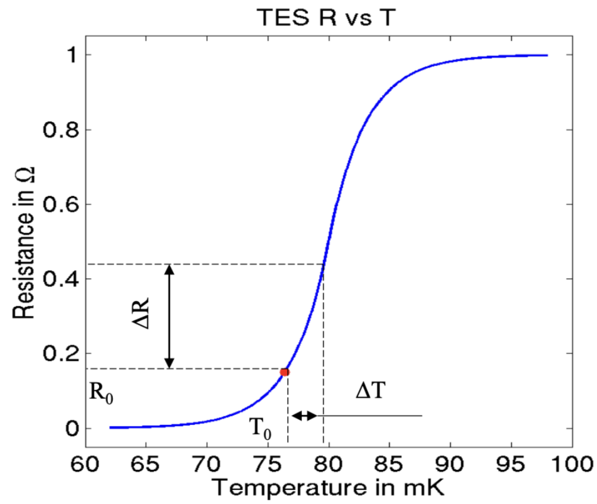

Figure 3-6. The transition resistance vs. temperature curve of a superconducting material is shown in the figure. In the transition region, the resistance is highly sensitive to temperature variations. This property allows the system to detect extremely small amounts of heat generated by potential dark matter interactions, making it an effective tool for precision measurements in cryogenic detectors. Credit: SuperCDMS collaboration

being small, requires only a few QETs to effectively collect phonon signals. This results in a smaller volume of tungsten TES, which lowers the heat capacity and increases sensitivity to small temperature changes, thereby achieving a lower energy threshold. In contrast, the larger surface area of the HV detector requires more QETs to cover the crystal effectively, which in turn necessitates more tungsten TES, increasing the heat capacity. This higher heat capacity reduces sensitivity to small energy deposits, leading to a higher energy threshold.

3.3 SQUID Circuit

The Superconducting Quantum Interference Device (SQUID) circuit monitors the resistance of the TES and generates a current signal for the data recording system. A simplified SQUID circuit diagram is shown in Figure 3-7. The circuit consists of two parallel sub-circuits: the TES circuit on the left and the SQUID operational amplifier circuit on the right, with the SQUID connecting both sub-circuits.

The TES is biased in its transition region by applying a bias current I_b to the TES circuit. When a particle deposits energy in the detector crystal, it induces a change in the TES resistance, which causes a variation in the TES circuit current. This small current variation generates a flux change within the SQUID loop, producing an additional voltage in the right sub-circuit. This voltage variation is then fed into the operational amplifier in the right sub-circuit, where it undergoes an amplification, enhancing the signal strength. The final amplified signal is output as V_{out} .

This amplification process enables the system to detect extremely small changes in the TES circuit with high sensitivity. The resulting electrical signal is recorded by the data acquisition system for further processing and analysis by researchers.

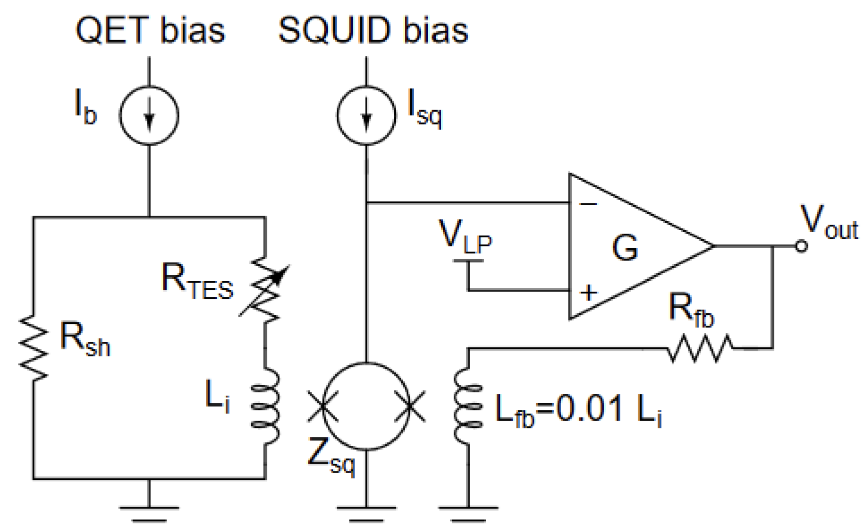

Figure 3-7. A simplified SQUID circuit diagram. The left side represents the TES subcircuit, which monitors variations in the TES resistance in response to energy deposition. The right side is the SQUID operational amplifier circuit, responsible for amplifying the signal generated by the TES subcircuit. The two subcircuits are interconnected through the SQUID device, enabling precise signal amplification and readout.

CHAPTER 4
SIGNAL MODEL

The SuperCDMS HVeV group focuses on detecting light dark matter (LDM), and as such, the signal model is designed to derive the scattering or absorption rates for various types of dark matter. This model incorporates not only the dark matter scattering and absorption effects but also detector-specific phenomena, such as electron trapping, ionization yield, and uncertainties in the production of electron-hole pairs. Consequently, the signal model acts as a bridge, linking the abstract physical processes of dark matter interactions with the detector to mathematical concepts that can be analyzed using statistical tools.

4.1 Dark Matter Models

The SuperCDMS HVeV program focuses on the search for LDM, considering both absorption and scattering interactions of LDM.

4.1.1 Absorption Model

The absorption model studied by the SuperCDMS HVeV group considers two types of dark matter candidates: the hidden photon and axion-like particles (ALPs). The model-independent equation describing the halo dark matter total absorption rate is:

$$R = \frac{1}{\rho}\frac{\rho_{\mathrm{DM}}}{m_{\mathrm{DM}}}\langle n_e \sigma_{\mathrm{abs}} v_{\mathrm{rel}}\rangle \, [18] \tag{4-1}$$

Where R is the total absorption rate of halo dark matter by a unit mass of detector target. Its unit depends on the chosen convention, with a common choice being $\frac{1}{g \cdot day}$. ρ is the mass density of the detector target, which, in the case of HVeV Run 4, corresponds to the mass density of silicon. ρ_{DM} represents the local dark matter mass density, and m_{DM} is the mass of a single dark matter particle. The term $\langle n_e \sigma_{\mathrm{abs}} v_{\mathrm{rel}}\rangle$ quantifies the dark matter total absorption rate by electrons in a material. Here, n_e is the electron number density in the material, σ_{abs} is the dark matter-electron absorption cross section, and v_{rel} is the relative velocity of dark matter particles within the local dark matter halo. Since v_{rel} follows a velocity distribution, the value of $\langle n_e \sigma_{\mathrm{abs}} v_{\mathrm{rel}}\rangle$ is obtained by calculating the expectation value over this distribution.

The dark matter-electron total absorption rate can be derived by relating it to the photon-electron total absorption rate. More details can be found in [18]. In this section, I will present a brief introduction to the two LDM models and the final dark matter particle total absorption rate relevant to the dark matter experiment.

For the case of the differential absorption rate $\frac{dR}{dE}$, the dark matter particles are assumed to be cold. As a result, their kinetic energy is negligible compared to their mass. This implies that the energy of the dark matter particles can be considered constant and approximately equal to their mass, leading to $\frac{dR}{dE} = \delta(E - m_{DM})$.

4.1.1.1 Dark Photon

The dark photon is a hypothetical gauge boson proposed as an extension to the Standard Model by introducing an additional $U(1)$ symmetry [16]. It can kinetically mix with the Standard Model photon and acquire mass via either the Higgs mechanism or the Stueckelberg mechanism. The relevant Lagrangian is:

$$\mathcal{L} \supset -\frac{\epsilon}{2} F_{\mu\nu} V^{\mu\nu} [18] \tag{4-2}$$

Here, $F_{\mu\nu}$ represents the field strength tensor of the photon, and $V^{\mu\nu}$ represents the field strength tensor of the hidden photon. The parameter ϵ is the kinetic mixing parameter, which quantifies the strength of kinetic mixing. The corresponding gauge boson, A^{μ} — known as the dark photon — can couple to the electromagnetic current J_{μ}^{EM} via the interaction term $\epsilon e A^{\mu} J_{\mu}^{EM}$ [16, 18]. The total absorption rate of dark photon by target is predicted by:

$$R = \frac{1}{\rho} \frac{\rho_{DM}}{m_{DM}} \epsilon_{eff}^{2} \sigma_1 (\omega = m_{DM}) [18] \tag{4-3}$$

Here, R, ρ, ρ_{DM} and m_{DM} retain the same meanings as defined in Section . The term σ_1 represents the real part of the complex conductivity of the detector material and is a function of the absorbed dark photon energy. The term ϵ_{eff}, known as the effective mixing angle [18], refers to the kinetic mixing parameter ϵ after accounting for in-medium effects, making it a medium-dependent parameter. To ensure consistency across different experiments, ϵ_{eff} is always converted back to ϵ for direct comparison. Figure 6-5 presents the constraints on the kinetic mixing parameter ϵ from HVeV Run 4.

4.1.1.2 Axion-Like Particle

Consider a pseudoscalar a - axion-like particle that directly couples to electron through the following Lagrangian term:

$$\mathcal{L} \supset \frac{g_{ae}}{2m_e}(\partial_\mu a)\bar{e}\gamma^\mu\gamma^5 e[18] \tag{4-4}$$

Here m_e and e is the mass and charge of an electron. The term g_{ae}, known as the effective coupling [18], is the parameter being targeted in dark matter experiments. Figure 6-5 shows the constraints on g_{ae} derived from the HVeV Run 4. The total absorption rate of axion-like particle by target is predicted by:

$$R = \frac{\rho_{\mathrm{DM}}}{\rho}\frac{3m_{\mathrm{DM}}}{4m_e^2e^2}g_{ae}^2\sigma_1(m_{DM})[18] \tag{4-5}$$

Here, R, ρ, ρ_{DM} and m_{DM} retain the same meanings as defined in Section . The term σ_1 represents the real part of the complex conductivity of the detector material and is a function of the absorbed axion-like particle energy.

4.1.2 Scattering Model

Unlike the absorption model, the scattering model assumes that dark matter particles scatter off electrons, transferring energy and momentum to ionize electrons into the conduction band, without the loss of dark matter particles. Various scattering dark matter models consider particles with masses in the typical energy range of light dark matter (LDM), spanning from keV to GeV. Examples include WIMPless, asymmetric dark matter, bosonic super-WIMP, Axino, gravitino, and sterile neutrino dark matter [15], etc.

Equation 4-6 predicts the scattering rate of such kinds of dark matter particles within silicon or germanium crystal. For more details, readers can refer to the paper [14].

$$\frac{dR}{d\ln E} = \frac{\rho_\chi}{m_\chi} N_{\text{cell}} \sigma_e \alpha \cdot \frac{m_e^2}{\mu_{\chi e}^2} \int d\ln q \left(\frac{E}{q} \eta \left(v_{\min}(q, E) \right) \right) F_{\text{DM}}(q)^2 \left| f_{\text{crystal}}(q, E) \right|^2 \text{[14]} \quad (4\text{-}6)$$

Here, E represents the recoil energy deposited by the dark matter particle, and q is the momentum transfer between the dark matter particle and the electron. The term ρ_χ denotes the local dark matter density, while m_χ is the mass of the dark matter particle. The term $N_{\text{cell}} = \frac{m_{target}}{m_{\text{cell}}}$ is the number of unit cells in the crystal target, defined as the ratio of the total target mass to the mass of a single unit cell of the crystal. The parameter σ_e represents the dark matter-electron scattering cross section, and α is the fine structure constant. m_e is the mass of the electron, and $\mu_{\chi e}$ is the reduced mass of the dark matter particle and the electron.

The integral accounts for the contributions from all possible momentum transfer values, as the momentum transfer can vary across different scattering events. The term $v_{\min}(q, E)$ is the minimum velocity of a dark matter particle required to produce a scattering event with a momentum transfer q and recoil energy E. The function $\eta(v_{\min}(q, E))$ encodes the information about the dark matter velocity distribution, integrating over velocities that exceed $v_{\min}(q, E)$.

The term $F_{\text{DM}}(q)$, known as the dark matter form factor, modifies the scattering strength between dark matter particles and electrons for different dark matter models as a function of momentum transfer q. For instance, $F_{\text{DM}}(q)$ can be 1 for heavy vector mediator exchange, proportional to $\frac{1}{q}$ for electric dipole moment coupling, or proportional to $\frac{1}{q^2}$ for the exchange of a massless or ultra-light vector mediator [14]. The final term, $f_{\text{crystal}}(q, E)$, represents the crystal form factor, which accounts for the contributions of the crystal's electronic structure to the scattering process [14]. Thus, the Equation 4-6 depends on both the dark matter model and the type of crystal.

4.2 Pair Production Model

The SuperCDMS HVeV experiment and the high-voltage (HV) detectors in the SuperCDMS SNOLAB experiment utilize the Neganov-Trofimov-Luke (NTL) effect to amplify the weak recoil energy from incident particles. As illustrated in {add reference chapter}, the process can be described by the equation:

$$E_{ph} = E_r + n_{eh} \cdot e \cdot V_{bias} \tag{4-7}$$

Where E_{ph} is the total phonon energy, E_r is the recoil energy of the initial particle, n_{eh} is the number of electron-hole pairs generated, e is the elementary charge, and V_{bias} is the bias voltage across the detector absorber.

In a realistic dark matter experiment, researchers measure the total phonon energy E_{ph} with the detector and use the number of electron-hole pairs n_{eh} to reconstruct the recoil energy E_r. However, n_{eh} is not a simple, directly derived quantity, it is actually a distribution that depends on the recoil energy. Therefore, to accurately reconstruct the recoil energy, it is important to precisely build the parameter n_{eh}. The pair production model aims to provide an accurate estimate of the distribution of n_{eh}.

4.2.1 Simple Model

Three parameters are involved in the simple model. As mentioned before, n_{eh} is the number of electron-hole pairs generated, and E_r is the recoil energy (or called deposited energy) of the initial particle. The parameter ϵ_{eh} is the average energy required to generate an electron-hole pair in a crystal. Equation 4-8 shows how to calculate the number of generated electrons and holes.

$$n_{eh} = \frac{E_r}{\epsilon_{eh}} \tag{4-8}$$

In principle, ϵ_{eh} is energy-dependent; its value varies at low energy ranges and becomes stable at high energies. In the simple model, the value of ϵ_{eh} is simplified to $\epsilon_{eh,\infty}$ (if the recoil energy is high enough the value of ϵ_{eh} is stable at $\epsilon_{eh,\infty}$). Furthermore, parameter ϵ_{eh} is a statistical average value, thus the real number of electron-hole generated n_{eh} is different each time, however the simple model treats this average as a constant value occurring every time, ignoring fluctuations in the actual number each time the pair production process happens. This simplified model provides a poor approximation to real physics. However, it offers good intuition for understanding the pair production process, forming the basis for more complex models such as the binomial model and the R-K model.

4.2.2 Binomial Model

In HVeV Run 1 and Run 2, an improved model—the binomial model—was used to reconstruct the recoil energy from the measured phonon energy. Unless the simple model, the binomial model incorporate the energy dependence effect of parameter ϵ_{eh}, it also consider the value of generated electron-hole pairs n_{eh} as a random variable at large energy. Equation 4-8 still hold for binomial model, however parameters n_{eh} and ϵ_{eh} is having energy dependence - $n_{eh}(E_r)$ and $\epsilon_{eh}(E_r)$, furthermore parameter $n_{eh}(E_r)$ becomes a random variable at high energy instead of a constant number. $\epsilon_{eh}(E_r)$ have three different value based on the recoil energy in binomial model:

1. $E_r < E_{gap}$: when the recoil energy is insufficient to overcome the band gap of the absorber crystal, no electron-hole pairs are generated, thus $\epsilon_{eh}(E_r)$ is infinite large - ∞.

2. $E_{gap} < E_r < \epsilon_{eh,\infty}$: if the recoil energy exceeds the band gap but is less than the high energy value of mean pair creation energy $\epsilon_{eh,\infty}$, only a single electron-hole pair is produced, thus $\epsilon_{eh}(E_r) = E_r$.

3. $\epsilon_{eh,\infty} < E_r$: when the recoil energy surpasses the high energy value of mean pair creation energy, then $\epsilon_{eh}(E_r) = \epsilon_{eh,\infty}$, and the number of electron-hole pairs follows a binomial distribution with a mean value of $\frac{E_r}{\epsilon_{eh,\infty}}$.

The simple model Equation 4-8 thus evolves into:

$$\langle n_{eh}(E_r)\rangle = \begin{cases} 0, & E_r < E_{gap}, \\ 1, & E_{gap} < E_r < \epsilon_{eh,\infty}, \\ \frac{E_r}{\epsilon_{eh,\infty}}, & \epsilon_{eh,\infty} < E_r, \end{cases} \tag{4-9}$$

As recoil energy E_r larger than mean pair ionization energy ϵ_{eh}, this model interprets the generation of electron-hole pairs as resulting from n independent ionization attempts, each with a probability p of success. According to the properties of the binomial distribution, the mean number of ionized electron and hole pairs are $\mu = np = \frac{E_r}{\epsilon_{eh,\infty}}$. To build a complete binomial model, a factor which relate the mean and variation of binomial distribution, called Fano factor F, is required. The Fano factor is defined as $F = \frac{\sigma^2}{\mu}$, where σ^2 is the variance and μ is the mean of the binomial distribution. The value of the Fano factor can be determined experimentally or obtained from relevant literature. The variance of the binomial distribution can be expressed as $\sigma^2 = F \cdot \frac{E_r}{\epsilon_{eh,\infty}} = np(1-p)$. The variance σ^2, together with the mean number of ionized electron-hole pairs μ, fully characterizes a binomial distribution.

4.2.3 RK Model

The binomial model introduces statistical variation into the calculations, optimizing the pair production estimation. However, it still oversimplifies the value of $\epsilon_{eh}(E_r)$ at low recoil energies E_r. A phenomenological model presented by Ramanathan and Kurinsky [28], referred to as the RK model within the HVeV group, was used in HVeV Run 3 and Run 4. This model applies Monte Carlo simulations to derive the pair creation probability distribution.

The derived pair creation probability distribution of the RK model is shown in Figure 4-1. The pair creation probability as a function of recoil energy is plotted for three different temperatures: 0K, 100K, and 300K. During HVeV data analysis, the temperature parameter is mapped onto the band gap energy, thus, the three different temperatures correspond to three different band gap energies. To derive the probability at arbitrary temperatures, the temperature is first converted to band gap energy, and then an extrapolation method is applied based on the provided data at the three band gap energies corresponding to 0 K, 100 K, and 300 K.

Beyond the pair creation probability used in the data analysis, the physics behind the RK model follows the same principles as the simple model and the binomial model. However, the RK model provides an extension that addresses the limitations of these two naive models. Parameter $\epsilon_{eh}(E_r)$ in the RK model obeys the following Equation 4-10:

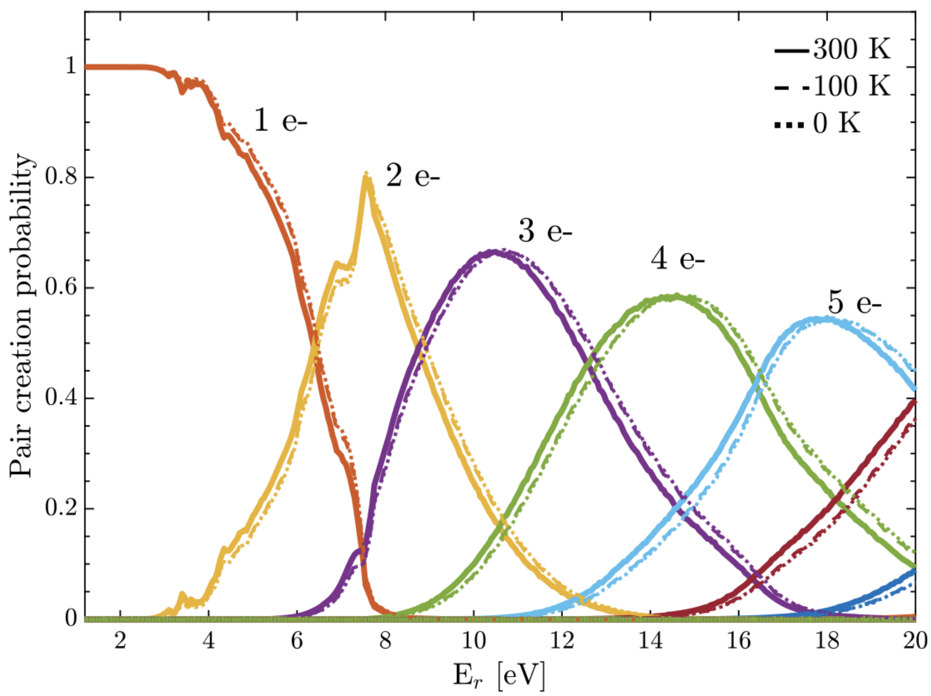

Figure 4-1. Pair creation probability as a function of deposited energy at different temperatures, based on the RK model. Each color represents the probability of generating a specific number of electron-hole pairs. The temperature dependence is also illustrated in the figure, with solid, dashed, and dotted lines corresponding to 300 K, 100 K and 0 K. Credit: [28].

$$\epsilon_{eh}(E_r) = \begin{cases} \infty, & E_r < E_{gap}, \\ E_r, & E_{gap} \le E_r \le 2E_{gap}, \\ \epsilon_{imp}(E_r), & E_r \ge 2E_{gap}, \\ \epsilon_{eh,\infty}, & E_r \to \infty \end{cases} \tag{4-10}$$

If recoil energy smaller than the band gap energy, no electron-pair can be generated. Different with the binomial energy, RK model set the $\epsilon_{eh}(E_r) = E_r$ as recoil energy between band gap energy and two time band gap energy. If recoil energy is high enough, the mean pair ionization energy $\epsilon_{eh}(E_r)$ stable to its high energy value $\epsilon_{eh,\infty}$. The RK model introduce an intermediate function $\epsilon_{imp}(E_r)$ that smoothly connect to the low energy value and high energy of $\epsilon_{eh}(E_r)$. Besides the mean pair production energy $\epsilon_{eh}(E_r)$, the Fano factor is also an energy dependence value, whose functional form is shown in the following Equation 4-11.

$$F(E_r) = \begin{cases} 0, & E_r \le 2E_{gap}, \\ F_{imp}(E_r), & E_r \ge 2E_{gap}, \\ F_\infty, & E_r \to \infty \end{cases} \tag{4-11}$$

When $E_r \le 2E_{gap}$, the number of pair production is constant at 0 or 1 based on the energy, as illustrated in Equation 4-10. If $E_r \to \infty$, the Fano factor is stable at its high energy value and the value can be either measured or quoted from relevant literature. For the in between energy range, $F(E_r) = F_{imp}(R_r)$, and $F_{imp}(R_r)$ is a unknown function that smoothly connect the low energy of $F(E_r) = 0$ and high $F(E_r) = F_\infty$. The detailed information of $\epsilon_{imp}(E_r)$ and $F_{imp}(R_r)$ and the Monto-Carlo simulation used here can be checked in the original paper [28].

4.3 Charge Trapping and Impact Ionization Model

When an energetic particle scatters from or is absorbed by the crystal absorber, electron-hole pairs are generated. Due to the bias voltage, electrons and holes drift toward the crystal surfaces. And these process can be governed by the pair creation model and Equation 4-7. However, during the motion of electron and hole, they can be trapped within the crystal bulk or on the crystal surface; this effect is referred to as charge trapping. Simultaneously, a carrier can ionize another charge carrier during its transport—a phenomenon known as impact ionization. Thus the number of electron and holes n_{eh} provided by the pair production model can't be directly used in Equation 4-7, it have to incorporate the consideration of charge trapping effect and impact ionization effect.

The charge trapping and impact ionization model—referred to as the CTII model in this section—aims to quantify these two effects with a probability density function. The HVeV group developed the flat model as the initial version of the CTII model. This flat model mathematically describes the physical processes of charge trapping and impact ionization, establishing the fundamental principles for solving related problem. Building upon the flat model, the latest version of the CTII model is the exponential model. This model, accounts for higher-order processes (multiple times of CTII process happen) and incorporates more detailed physics, thereby overcoming the limitations of the flat model.

4.3.1 Flat Model

In flat model, behavior of individual each electron-hole pair is assumed to be independent of other pairs. And when a pair is transferring within the crystal, the probability of trapped or ionized new pairs is constant or flat which is the origin of name flat model. Flat model consider three situations [25]:

1. A_{-}: charge trapping probability
2. A_{+}: impact ionization probability
3. $1 - A_{-} - A_{+}$: probability for pair reaching to crystal surface unhindered

Thus the probability density function $h(x)$ of a single electron-hole pair can be expressed as:

$$h(x) = A_{-}\Theta(x-0)\cdot\Theta(1-x) + A_{+}\Theta(x-1)\cdot\Theta(2-x) + A_{I}\delta(x-1) \tag{4-12}$$

Where x is the the measured energy normalized to number of electron-hole pairs, the $\Theta(x)$ is Heaviside function, $\delta(x)$ is Dirac delta function.

To deal with the case of multiple electron-hole pairs generated at the same time, flat model extend the probability density function of a single electron-hole pair to multiple electron-hole pairs with convolution. The convolution appearing here is a mathematical trick to allocate coefficient of each term.

$$^{(m)}h(x) = \int_{-\infty}^{\infty} {}^{(1)}h(x') \cdot {}^{(m-1)} h(x - x')\, dx' \tag{4-13}$$

The flat model is the first version of the CTII model, providing researchers with a quantitative tool to understand the effects of charge trapping and impact ionization. However, the flat model oversimplifies the underlying physics, and as research progresses, its accuracy becomes insufficient. More advanced models are required for deeper investigations.

4.3.2 Exponential Model

4.3.2.1 Formulation

The exponential model [35] is an extension of the flat model, it is designed to provide better accuracy and solve for more complex physics condition. Comparing with the flat model, the exponential model have several important improvements. First of all, the formulation of exponential model reveals that the probabilities of charge trapping (CT) or impact ionization (II) decay exponentially with the thickness of the detector, i.e. it is a function of charge position relative to the detector thickness. Let p denote the probability of a certain process occurring per unit distance as the charge travels along the z-axis. If a charge travels a distance of Δz, dividing it into n segments, the probability of the charge undergoing a specific process in each segment is $p\frac{\Delta z}{n}$. Therefore, the probability that no CT or II processes occur over the distance Δz is given by Equation 4-14.

$$\overline{C}_i(\Delta z) = \lim_{n\to\infty}\left(1 - p\frac{\Delta z}{n}\right)^n = e^{-p\Delta z} = e^{-\frac{\Delta z}{\tau}} \tag{4-14}$$

Where the parameter τ is the characteristic length of a certain process. The exponential model considers six different CT and II processes: electron trapping (CTe), hole trapping (CTh), creation of a hole by an electron (IIeh), creation of an electron by an electron (IIee), creation of an electron by a hole (IIhe), and creation of a hole by a hole (IIhh). Thus the each of a process can be allocated by a probability p and τ. The exponential model thus have the abilities to distinguish different CT and II process, and treat electrons and holes differently.

4.3.2.2 Basic Process

Based on the formulation from 4-14, basic CTII processes can be built. A basic CTII refereed here is a process up to second times of CT or II. Instead of presenting the mathematical details, an example of a particular case of basic CTII process is shown in the Figure 4-2. An electron and hole pair is generated at the middle of detector bulk, then the electron and hole are drifted to the direction of top and bottom crystal surface respectively, due to the applied electron field. During the transportation, the original electron impact ionize another hole, the new generated hole then reached to the bottom surface. The original hole trapped during its moving. The process described above is a particular basic CTII process, due to the position of impact ionization and charge trapping happened in the basic CTII process, the final measured energy obeys a probability distribution, the distribution function of such process is shown in Figure 4-3. For mathematical representation, reader can check paper [35].

4.3.2.3 Probability Density Function for Single and Multiple Electron-Hole Pair

For a dark matter event, electrons and holes are generated within the bulk of the detector crystal, and there are 16 unique basic CTII processes that need to be considered. The probability density function $F^{(1)}$, corresponding to a single electron-hole pair undergoing a general CTII process, can be constructed by combining the 16 basic CTII processes together. Once the probability density function for a single electron-hole pair experiencing a general CTII process is built, it can be convolved with itself $j-1$ times to produce the probability density function for j electron-hole pairs undergoing the general CTII process $F^{(j)}$. The process can be expressed as $F^{(j)}(n_{eh}) = F^{(j-1)}(n_{eh}) * F^{(1)}(n_{eh})$.

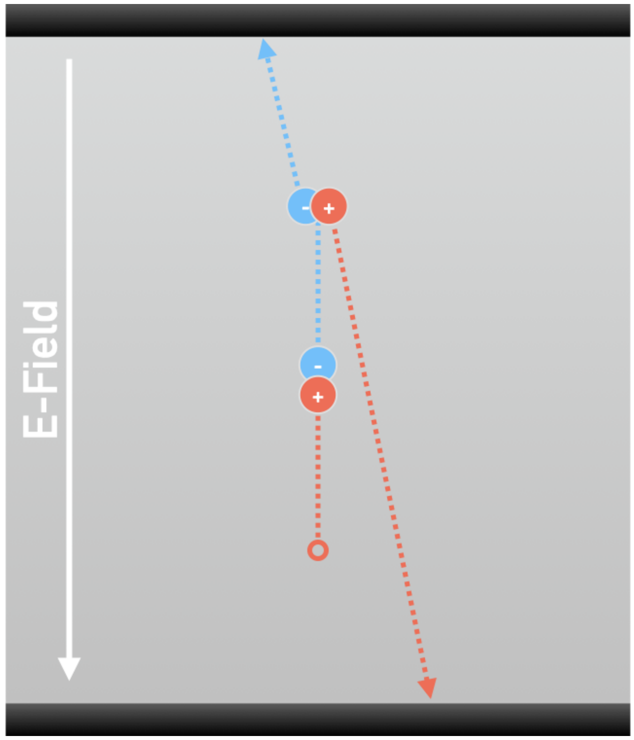

Figure 4-2. This figure illustrates a specific CTII process, in which an electron impact-ionizes a hole. The electron and the impacted hole reach the detector surface, while the original hole becomes trapped. Credit: Matthew Wilson, SuperCDMS internal documents.

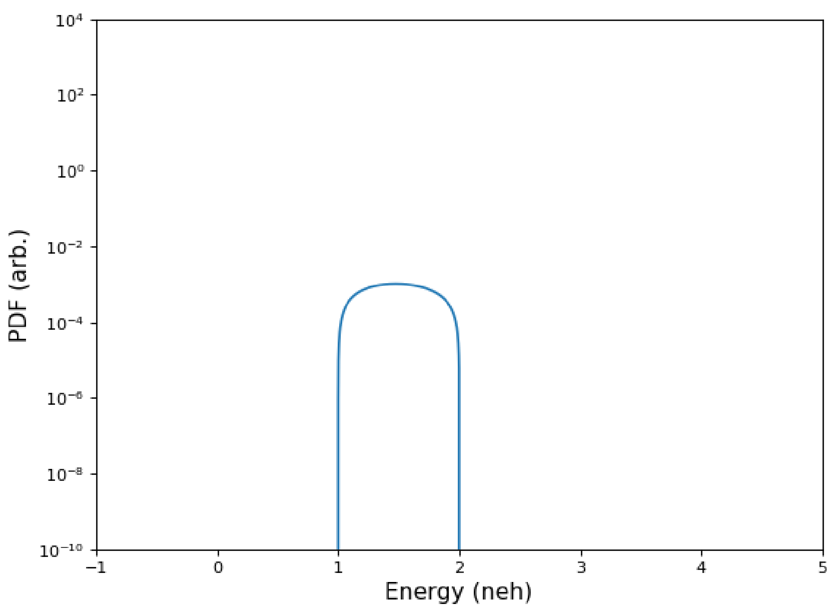

Figure 4-3. Probability density function of the CTII process shown in Figure 4-2. Credit: Matthew Wilson, SuperCDMS internal documents.

4.4 General Signal Model

The scattering or absorption of a dark matter particle by the detector crystal is considered a rare event, with an extremely low interaction frequency. Therefore, a dark matter event is treated as a single-hit event, in contrast to LED or laser energy calibration data, where multiple hits can occur simultaneously. For more information on the theory and data related to multiple hits, refer to the paper [35]. A single-hit event can produce a random number of electron-hole pairs. Therefore, the final probability density function for the energy of a dark matter single-hit event must account for all possible numbers of electron-hole pairs. This can be described by the following equation:

$$H(E_{\text{ph}}) = \sum_{j=1}^{J} \left(\int_{0}^{\infty} dE_{\text{dep}}\, p_{\text{eh}}(j|E_{\text{dep}}) \times \frac{F^{(j)}\left(\frac{E_{\text{ph}}-E_{\text{dep}}}{eV_{\text{bias}}}\right)}{eV_{\text{bias}}} \cdot \frac{d\bar{R}}{dE_{\text{dep}}}(E_{\text{dep}}) \right) [35] \tag{4-15}$$

The total measured phonon energy, E_{ph}, can be converted to n_{eh} using Equation 4-8. The term $p_{\text{eh}}(j|E_{\text{dep}})$ represents the probability that j electron-hole pairs are created when dark matter deposits energy E_{dep} into the crystal. The term $F^{(j)}\left(\frac{E_{\text{ph}}-E_{\text{dep}}}{eV_{\text{bias}}}\right)$ is the probability density function for j electron-hole pairs undergoing a general CTII process. Parameter conversion from n_{eh} to E_{ph} yield a term $\frac{1}{eV_{bias}}$. The term $\frac{d\bar{R}}{dE_{\text{dep}}}(E_{\text{dep}})$ is the normalized dark matter energy deposition spectrum, which varies depending on the dark matter model. More details can be found in paper [35].

The function $H(E_{\text{ph}})$ is the probability density function of measured phonon energy for dark matter events. To fully recover the dark matter differential absorption or scattering rate over measured phonon energy, one need ratio the function $H(E_{\text{ph}})$ with dark matter interaction rate R:

$$\text{Differential rate} = R \cdot H(E_{\text{ph}}) \tag{4-16}$$

Where R is total dark matter interaction rate - in $\frac{1}{g \cdot day}$, it is values varies for different dark matter mass and it is also dependent the specific dark matter model using. The value of R can be produced by the dark matter models described in the beginning part of this chapter.

CHAPTER 5
BACKGROUND EVENTS

5.1 Cosmic Ray Induced Background

Cosmic rays are high-energy elementary particles and nuclei that originate from various sources, including supernova explosions, black holes, and other astrophysical phenomena in the universe. The specific composition of cosmic rays varies with energy. While nuclei, especially hydrogen (protons) and helium, overwhelmingly dominate, the remainder consists of a small portion of heavier nuclei and electrons.

Cosmic rays from outer space are not considered background signals because their extremely high energy typically falls outside the energy region of dark matter recoils and can be easily distinguished. Furthermore, high-energy nuclei and electrons are effectively absorbed by the atmosphere, preventing them from reaching ground. However, cosmic rays from outer space can interact with the Earth's atmosphere, generating a series of secondary particles that can directly or indirectly impair the sensitivity of dark matter experiments.

High-energy nuclei interact with atmospheric nuclei, producing mesons, including charged kaons, charged pions, and neutral kaons and pions. These mesons can either decay or collide with other atmospheric nuclei, generating subsequent generations of particles such as muons, neutrinos, electrons, positrons, photons, etc. Figure 5-1 illustrates the vertical flux of major components related to cosmic rays at different altitudes. As shown in this figure, particle flux is greatly attenuated as these particles pass through the atmosphere. However, even though only a small fraction of particles reaches ground level, dark matter search experiments built with extremely high sensitivity can still inevitably capture signals from such particles. These signals can potentially mimic dark matter interactions, producing false positives in the experiments.

Modern dark matter direct detection experiments are conducted deep underground, utilizing rock overburden to further reduce particle flux. This rock shielding effectively eliminates the influence of particles with large interaction cross-sections induced by cosmic rays, including protons, photons, electrons, etc. Only muons and neutrinos can penetrate into underground laboratories, becoming irreducible background sources either through direct interactions or

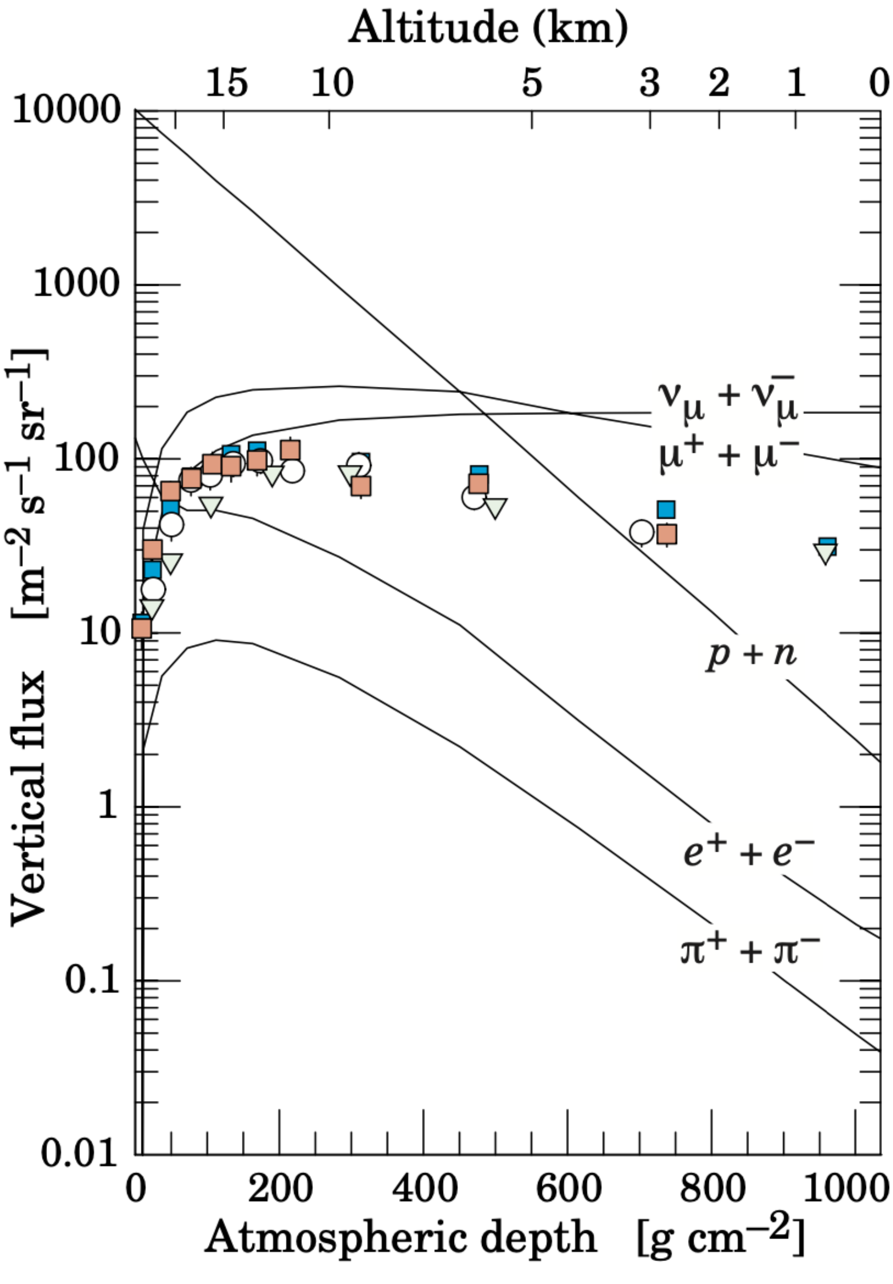

Figure 5-1. The vertical fluxes of the outer space cosmic-ray and its secondary particles components in the atmosphere in the energy region where the particles are most numerous (except for electrons, which are most numerous near their critical energy, which is about 81 MeV in air). Credit: [36].

indirect effects. Besides attenuating particles, rock overburden also isolates detectors from human and natural activities, such as shielding against electromagnetic radiation and minimizing temperature variations, providing a stable detection environment.

5.1.1 Muons

Muons induced by cosmic rays, referred to as cosmic-ray muons in this section, can inflict non-negligible negative effects on dark matter direct detection. One of the most significant concerns is that cosmic-ray muons can interact with rocks, lab materials, etc., inducing neutrons through several interactions such as negative muon capture and direct muon-induced nucleus spallation, etc. [27] These neutrons create indistinguishable backgrounds for dark matter searches. Additionally, cosmic-ray muons can directly interact with the detector absorber, depositing a large amount of energy, which increases the detector's dead time—the period when the detector cannot record events—thereby reducing the detector's exposure.

Cosmic-ray muon flux decreases dramatically with depth. As muon particles pass through the overburden, they lose energy through ionization and radiative processes. Thus, building deep underground laboratories is the most effective method to shield muon particles. Figure 5-2 demonstrates the cosmic-ray muon flux measured at laboratories worldwide, together with Monte Carlo simulation results.

Besides overburden passive shielding, an active veto system is also applied in many dark matter experiments to exclude signals related to cosmic-ray muons. For instance, the SuperCDMS Soudan experiment utilized a 5 cm thick muon scintillator veto system encompassing the detector [30]. When a muon passes through the scintillator, the veto system tags the muon interaction time and position. Researchers can then reject signals in the detector absorber that are highly correlated with the tagged muon events.

5.1.2 Neutrinos

Neutrino is another irreducible background particles, due to its extremely small scattering cross-section, there is no existing method to shield it. Neutrino particles can thus pass through underground laboratory, and getting scattered by detector absorber, producing mimic dark matter

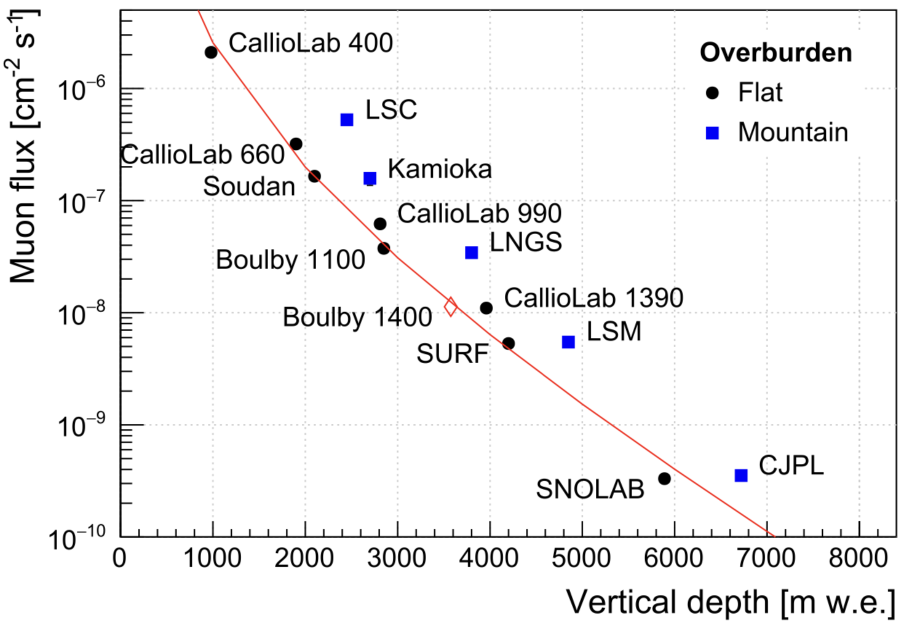

Figure 5-2. Muon flux as a function of vertical depth in meters water equivalent (m. w. e.) for different laboratories. Blue squares represent measurements of laboratories under relative flat surfaces and under mountain surfaces. The red curve is result of Monte Carlo simulations [27].

signals. As shown in Figure 2-4, the blue shaded region at the bottom is the region where neutrinos become the dominant source, and it is difficult to distinguish from dark matter signals, the neutrino background is referred to as “neutrino fog” or “neutrino floor”. The impact of neutrino background will become significant in the near future, since the next generation of ark matte direct experiment will have enough sensitivity to touch the neutrino fog.

Atmospheric neutrinos, originating from the interaction chain of cosmic rays, along with solar neutrinos and diffuse supernova neutrinos, constitute the neutrino fog in dark matter experiments. The precise impact of the neutrino background on each experiment can vary with neutrino energies, target materials, dark matter candidate mass, etc. For example, solar pp-neutrinos are an important source of electronic recoil background which is relevant to SuperCDMS experiments, while solar ^{8}B and atmosphere neutrinos can impact light and heavy dark matter searches, respectively [22].

5.1.3 Cosmogenic Activation

Cosmic rays and their secondary high-energy particles can generate radioisotopes through interactions with detector materials, a phenomenon known as cosmogenic activation. All materials used in dark matter experiments, including silicon and germanium targets as well as common construction materials like copper, lead, and stainless steel, are susceptible to this process.

Materials should be handled with extreme care during production, transportation, and installation to minimize exposure to cosmic rays and thus reduce radiation levels. Furthermore, placing materials underground for an extended period can effectively lower their radiation levels, as most radioisotopes generated by cosmic rays have relatively short half-lives.

5.2 Radioactive Background

Radioactive background can be pervasive in every part of an underground laboratory, including the rock, concrete walls, detector materials, and even within the detector absorber and shielding materials. Unlike cosmogenic activition background, natrually occurring radioisotopes typically have very long half-life thus should be considered as permanent background sources. The standard approach to mitigate this background involves using materials such as lead and copper to isolate the detector target from its surroundings. However, the radiation level of shielding material should be take extra care. As a general principle, the closer the material is to the detector target, the lower the radiation level should be.

Radioactive processes commonly produce alpha particles, electrons, positrons, gamma rays, and neutrons. Alpha particles and electrons, which lose energy rapidly through ionization, have short ranges and can be relatively easily shielded. In contrast, neutrons and gamma rays can travel long distances and reach the detector, producing low-energy nuclear or electron recoils, respectively [32], thus requiring more sophisticated handling.

Low-A materials (low mass number materials), such as polyethylene, water, can reduce neutron backgrounds effectively. While high-Z materials (high atomic number materials), such as lead is used to reduce the flux of gamma-ray. Thus the two kinds of materials are widely applied to dark matter direct detection experiments.

5.3 Background and Shielding Strategy in SuperCDMS Experiments

The SuperCDMS HVeV and SNOLAB experiments are conducted at MINOS at Fermilab and in Lively, Ontario, Canada, respectively. Both experiments utilize silicon or germanium as absorbers and copper for thermal conduction. Although the specific concentration of background radiation may differ due to the variations in location, the general types of background sources from the materials used are similar.

Radioactive backgrounds such as ^{238}U, ^{232}Th, and ^{40}K naturally occur and can emit beta particles and gamma rays during decay processes. These are present in the cavern walls of underground laboratories and are also introduced into detector components during manufacturing, including in the cryostat and electronic devices, etc. ^{222}Rn in the cavern environment is also considered an important background source. Dust containing ^{222}Rn can deposit on detector surfaces and emit beta and gamma particles [11].

Controlling exposure to cosmic rays is crucial. Neutrons, protons, and muons from cosmic rays can produce tritium (^{3}H) through spallation in both germanium and silicon detectors. Additionally, activation of the silicon absorber can introduce ^{32}Si, while the germanium absorber can lead to the production of ^{68}Ge, ^{68}Ga, ^{65}Zn, etc. Copper material, after exposure to cosmic ray-induced particles, can incorporate isotopes like ^{57}Co, ^{58}Co, and ^{60}Co, which are sources of gamma rays or beta particles, thereby causing electron recoil backgrounds and reducing the sensitivity of both the HVeV detector and the HV detector of SuperCDMS SNOLAB [11].

5.3.1 SuperCDMS HVeV

The SuperCDMS HVeV experiment utilizes HVeV detectors and operates as a subproject within the broader SuperCDMS collaboration, aiming to explore the parameter space of light dark matter (LDM). Following the success of the first two science runs, HVeV Run 3 and Run 4 were relocated to the MINOS facility at Fermilab. For more details about the HVeV facility and experiment setup, readers can refer to 6.2.

The SuperCDMS HVeV Run 3 to Run 4 were operated at a depth of 107 meters (225 m w.e.) underground, where the impact of muons is notable. However, the experiment was significantly affected by leakage events that originate from the bulk of the detector target or its surface. Consequently, the impact of muons or other atmospheric particles can be considered minimal. For this reason, the shielding for the SuperCDMS HVeV experiment is relatively simple, and no detailed background analysis has been conducted. The primary shielding consists of lead bricks that encase the detector, as shown in Figure 5-3, which helps reduce the flux of gamma rays—identified as the primary external background particle in the HVeV experiments. Regarding neutron background, given its relatively low flux, no special treatment is applied. The detector's stainless steel holder and copper cavity also provide moderate shielding, although this is not their primary purpose.

5.3.2 SuperCDMS SNOLAB

Unlike the SuperCDMS HVeV experiment, the experiment located at SNOLAB conducts a detailed analysis of background radiation and implements a variety of shielding strategies. The 2 km (approximately 6000 m w.e.) overburden at SNOLAB effectively reduces the muon flux. As depicted in Figure 5-2, SNOLAB possesses one of the lowest muon flux levels among the world's laboratories, thus eliminating the need for an extra active muon veto system in the SuperCDMS SNOLAB detector.

Figure 5-4 illustrates a diagram of the SuperCDMS SNOLAB shielding. The detector targets are enclosed by an outer neutron shield, a gamma shield, and an inner neutron shield. The outer neutron shield consists of 60 cm of water in stainless steel tanks, supplemented by a base of high-density polyethylene. The inner neutron shield comprises 40 cm of high-density polyethylene, while the gamma shield includes a 23 cm layer of lead. The detector target is encased in a copper holder, which not only facilitates thermal conductivity but also provides modest gamma shielding [23]. The magnetic shield just outside the copper protects the phonon sensors from Earth's magnetic field [11].

5.4 PCB Luminescence in HVeV

During the analysis of the HVeV Run 2 experimental data, a population of events was observed that exhibited pulse shapes different from the pulse template, even after applying the χ^2

Figure 5-3. The lead shielding used at NEXUS. During HVeV Run 4, these lead bricks surrounded the CryoConcepts dilution refrigerator to reduce gamma radiation. Polyethylene boards are also visible in the setup, providing additional shielding against neutron radiation.

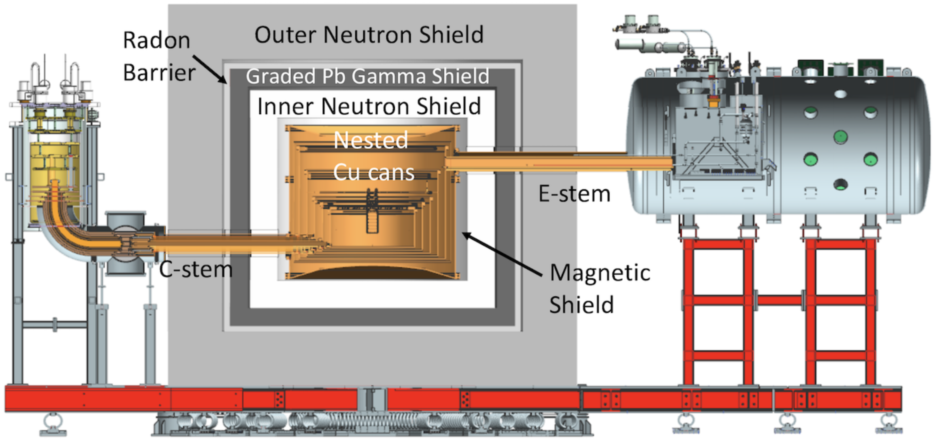

Figure 5-4. The detectors will be operated within a copper can, which is surrounded by multiple layers of shielding designed to reduce external background radiation. On the left side of the setup is a dilution refrigerator, which continuously maintains the detectors at cryogenic temperatures. The dilution refrigerator is connected to the detector housing via the C-stem (Cold stem), which provides thermal linkage. On the right side is the E-tank (Electronics tank), which houses the data readout system. The E-tank is connected to the detector housing through the E-stem (Electronics stem), ensuring signal transmission between the detectors and the readout electronics.

pulse shape selection. These events are referred to as burst events in this section. Burst events are apparent in both 0V data and high voltage (HV) data. At 0V, the pulses display a longer decay time compared to the pulse template. In the HV data, there is a significant number of events where more than one pulse is closely packed in time. Figure 5-5 presents the burst events at 60V. We theorize that the origin of these burst events is luminescence from the PCB [3].

During HVeV Run 3, four detectors were deployed, arranged in pairs. Detectors 1 and 2 are positioned adjacent to each other, as are Detectors 3 and 4. However, the pairs are separated and do not directly adjoin each other. Figure 5-6 shows the geometry of the four detectors. If the burst source is attributable to PCB luminescence, then events between two adjacent detectors sharing the same PCB should show a high correlation. Conversely, events occurring in detectors not mounted on the same PCB should lack such correlation.

Data analysis from HVeV Run 3 indeed observed such correlation between closely packed detectors, while no correlation was detected between detectors on different PCBs. Consequently, the detector holder was redesigned, replacing the PCB holder with a copper holder. After

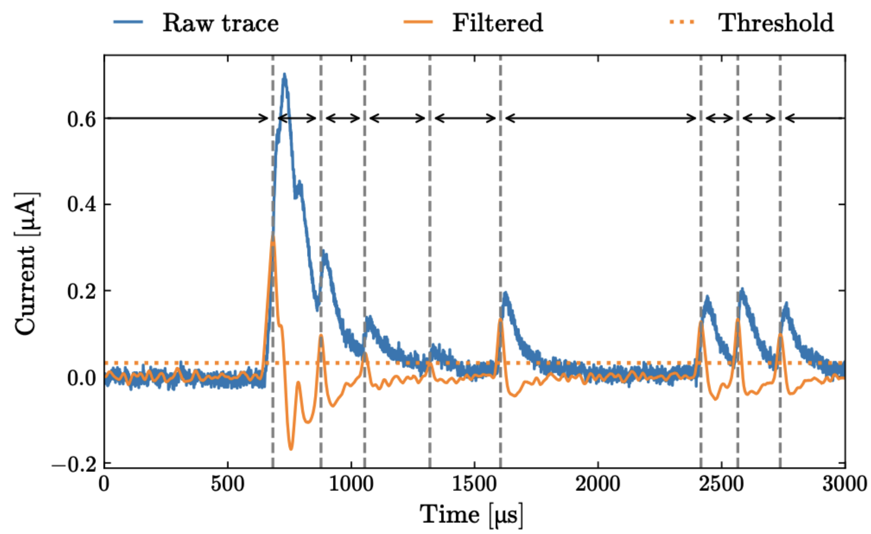

Figure 5-5. Burst events at 60 V: The blue curve represents the raw trace, while the orange curve shows the raw trace after applying a Gaussian derivative filter. The dotted orange line indicates the threshold used to select an event. The vertical dotted grey line marks the position of each event.

implementing the new copper holder, HVeV Run 4 data strongly validated the hypothesis of PCB luminescence, with a significant reduction in the background event rate observed.

5.5 Leakage Events

After resolving the issue of PCB luminescence, leakage events have become the dominant background. Researchers observed an unexpectedly high rate of single electron-hole pair events in the energy spectrum, while the rate for multiple electron-hole pairs remains low. This phenomenon is referred to as detector leakage.

The origins of leakage events are hypothesized to be electrons and holes spontaneously generated either within the crystal bulk or on the detector surface. A preliminary study on this topic has been conducted, considering several factors related to leakage rates, such as Al fin length, TES length, and voltage. The HVeV group also designed a new detector incorporating a layer of SiO_2 between the crystal and the QETs. However, no decisive conclusions have been reached yet, and the key factor that can reduce the leakage rate has not been identified. The study of leakage events continues.

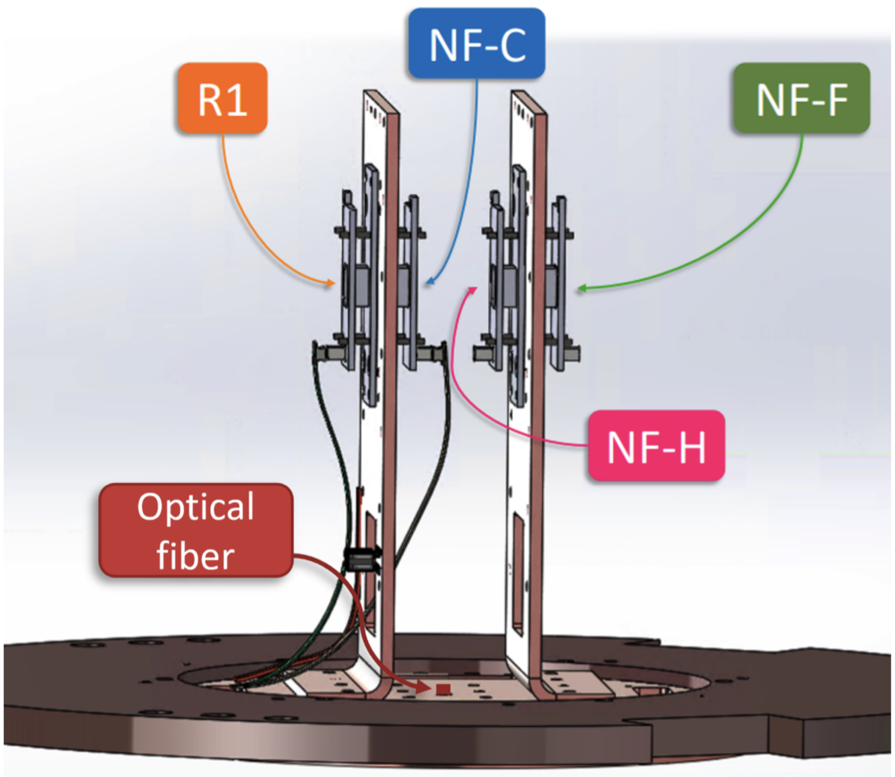

Figure 5-6. Detector geometry used in HVeV Run 3. Four HVeV detectors - R1, NF-C, NF-H and NF-F, were mounted on two copper holders. Each detector was clamped between two PCBs.[4]

5.6 Trigger Rate Spikes

After HVeV Run 3, a new phenomenon, referred to as the ’trigger rate spike’ or ’trigger rate jumping’, became more evident due to the lower background rate achieved by removing luminescent materials. According to the uniform dark halo model, the rate of dark matter scattering off a detector should remain constant over time. However, due to the trigger rate spike phenomenon, 1eh events rate can increase by 10 to 100 times in an instant, contradicting the uniform dark halo model. Subsequent studies revealed more details about this phenomenon, suggesting that it is most likely a detector background effect.

5.6.1 Properties

The phenomenon of a trigger rate spike was first discovered by its special shape in the trigger rate plot, as the example shown in Figure 5-7. During the process of a trigger rate spike, there are two distinct periods that characterize this phenomenon:

1. Fast changing period: The trigger rate can suddenly increase to 10 to 100 times higher than its stationary value almost instantly. After this sudden jump, the trigger rate can quickly decrease to a relatively small value, though it is still several times larger than the stationary value. This jumping and rapid decrease in the trigger rate forms a spike in the trigger rate plot. This period can last around half an hour.

2. Slow recovery period: After the fast changing period, the trigger rate gradually decreases to the stationary value. The excess trigger rate can be fitted by an exponential decay model during the slow recovery period. This period can last for around 10 hours. It is possible that the process can last even longer, but after around 10 hours, the excess event rate is low enough that it becomes indistinguishable from background events.

The trigger rate behavior throughout the entire process appears to follow a power law, expressed as $R = R_0 t^b$. In this model, the fast-changing period corresponds to the rapid decrease typically seen in the early stages of a power function, while the slow recovery period represents the characteristic long tail of the power function. Interestingly, a similar effect has been observed and studied in liquid xenon detectors at Purdue University. Although the underlying mechanisms may differ from those in cryogenic crystal dark matter experiments, a power-law rate behavior was also observed in their studies [19].

To investigate the origin of trigger rate spikes, further studies on this phenomenon were performed, and a series of properties of this phenomenon were discovered.

1. Coincidence with an exceptionally high-energy pulse: Each time the trigger rate spike phenomenon occurs, there is always an exceptionally high-energy pulse observed in the raw current, Figure 5-8 shows a typical exceptionally high-energy pulse. An exceptionally high-energy pulse is the actual starting point of the trigger rate spike phenomenon. All excess events introduced by the trigger rate spike appear only after the exceptionally high-energy pulse occurs. Therefore, the coincident exceptionally high-energy pulse has become a typical characteristic for identifying the trigger rate spike phenomenon, along with the two trigger rate periods discussed above. Furthermore, after estimating the energies of all high-energy pulses occurring in the detector, the trigger rate spike's high-energy pulses are found to have the greatest values among all high-energy events.

2. Single electron-hole (1eh) events only: The excess events introduced by the trigger rate spike phenomenon all have 1eh energy and can return a good value when compared with the pulse template using a chi-squared test. Which implies the excess events are all belongs to electron-hole pair events.

3. Localized events: As shown in Figure 5-9, the trigger rate spike excess events are confined within a relatively small portion on the y-axis. This indicates that these events are localized within a small region of the HVeV detector and are not spread over the entire detector.

4. Always occur: The trigger rate spike can occur at any time. Since the first discovery of the phenomenon, it has been found consistently during the HVeV detector operation.

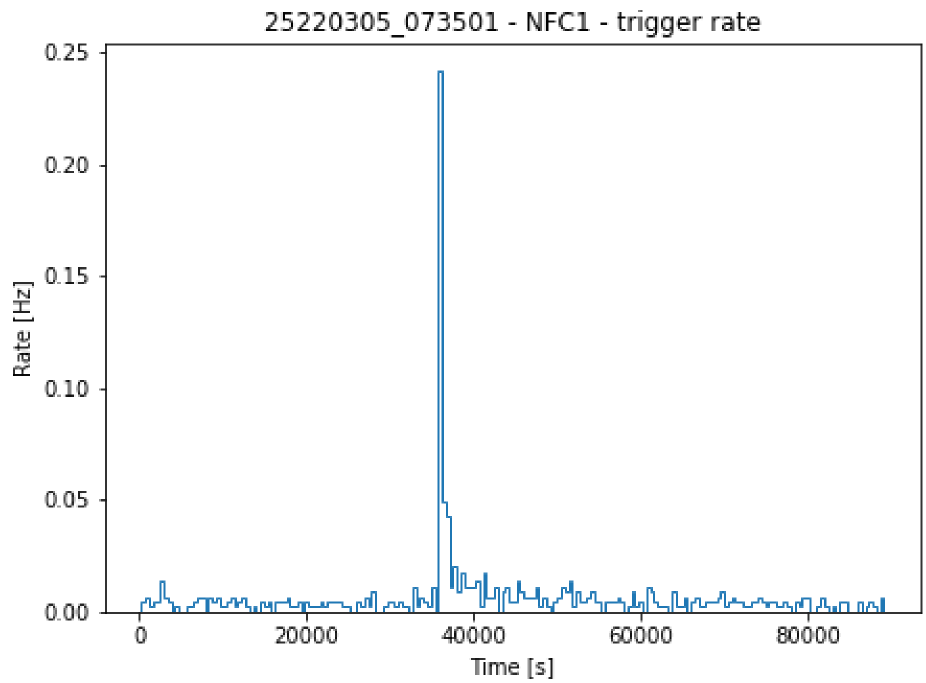

Figure 5-7. Trigger rate plot. The x-axis labels the time since the start of detector operation, and the y-axis represents the trigger rate. At around 36,000 seconds, a trigger rate spike occurs. The plot also shows the typical characteristics of the two periods mentioned in the Properties section. Since the start of the trigger rate spike, the first several bins experience the fast changing period, while after these bins, the trigger rate slowly recovers, belonging to the slow recovery period.

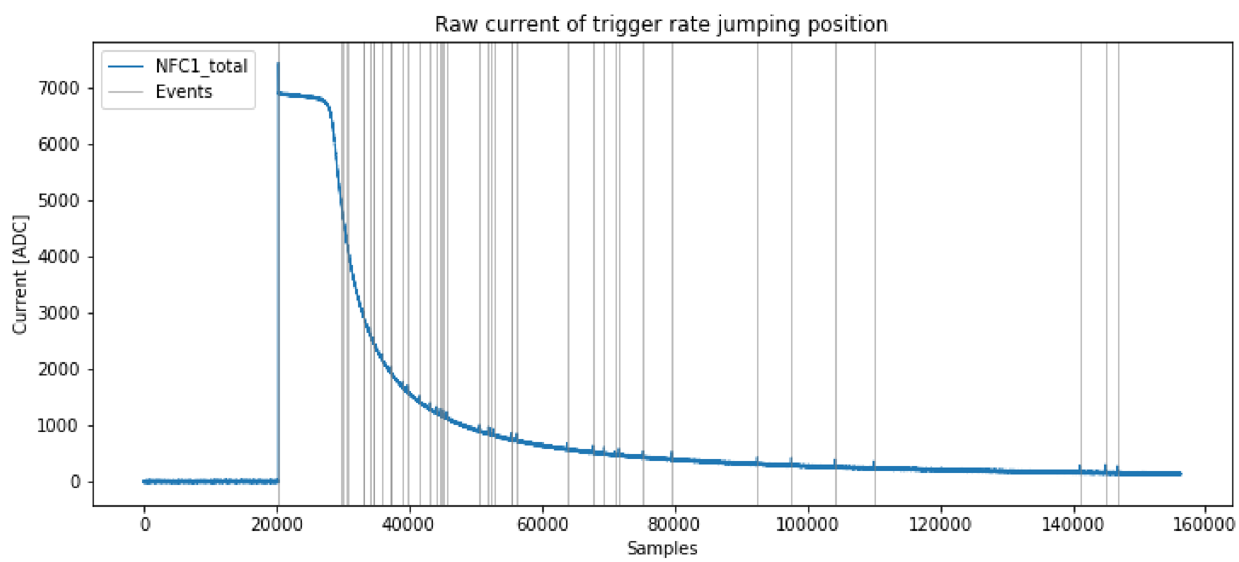

Figure 5-8. Exceptionally high-energy pulse. The x-axis represents the sample points, and the y-axis is the current in ADC units. The blue curve is the raw current, which contains an exceptionally high-energy pulse. The gray vertical line labels the excess 1eh events introduced by the trigger rate spike phenomenon.

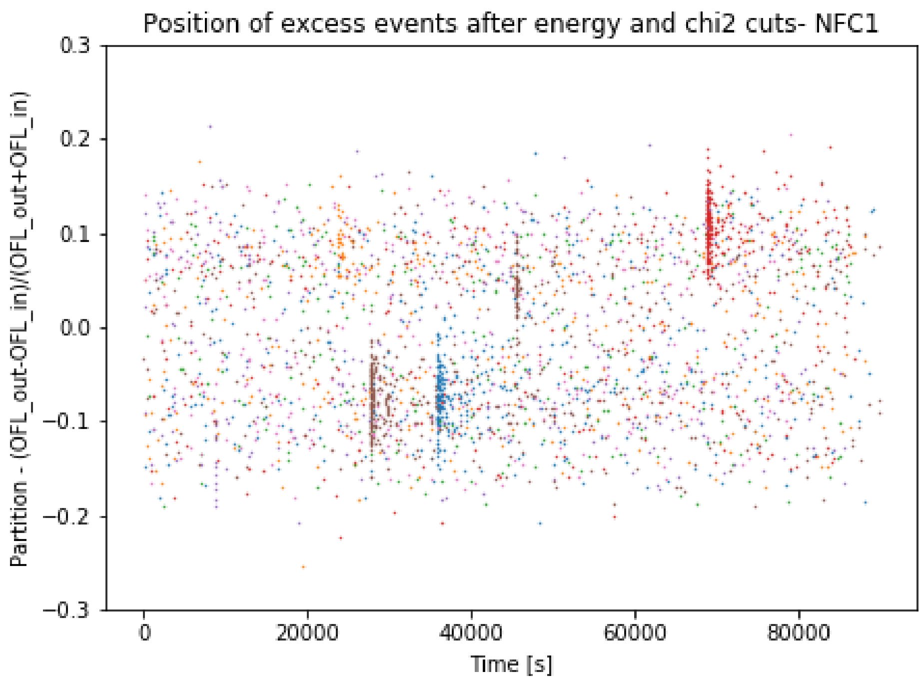

Figure 5-9. Localized events. The x-axis represents the time since the starting of data taken on each day, and the y-axis is the partition, which represents the relative amplitude of a signal received by the inner and outer channels. If it is greater than 0, the event is closer to the outer channel; if it is less than 0, the event is closer to the inner channel. Each dense region in the plot indicates the occurrence of the trigger rate spike phenomenon, which is localized relative to the outer and inner channels, thus demonstrating that the trigger rate spike phenomenon is localized. Points with different colors represent data collected on different days.

5. Can occur in all detectors: Since HVeV Run 3, the HVeV experiments have run on many different detectors, including both older and newer detectors. The trigger rate spike phenomenon can be found in all of them.

6. No coincidence between different detectors: The dilution fridge used by the HVeV experiment can be mounted with several different detectors. Each time a trigger rate spike phenomenon is observed in one detector, the same phenomenon is not found in the other detectors. This indicates that the probability of finding the phenomenon in a detector is independent of other detectors.

5.6.2 Are These Dark Matter Events?

First and foremost, before considering other possible explanations, we must ask: could these events be attributed to dark matter? Is there any specific reason to rule out the dark matter hypothesis?

To address this question, we must first review the characteristics of the trigger rate spike phenomenon. It begins with an extremely high-energy event, followed by a series of single-electron-hole (1eh) events whose rate gradually decreases over time. The entire process typically lasts around 10 hours. Two possibilities can be considered:

1. The extremely high-energy event is a dark matter interaction, while the subsequent 1eh events are caused by unknown detector effects. The trigger rate spike phenomenon occurs approximately once per day in a 1-gram silicon detector. This frequency implies that such high-energy events must involve particles with a large scattering cross-section. Moreover, the deposited energy of these events is extraordinarily high. If these events are triggered by dark matter particles, the implied large scattering cross-section would contradict the collisionless nature of dark matter. Additionally, such particles would have already been detected by other dark matter experiments with higher energy thresholds.

2. The hypothesis that the 1eh events following the extremely high-energy event are induced by dark matter also faces significant challenges. Firstly, this hypothesis cannot reconcile the

occurrence of the initial extremely high-energy event. There is no specific reason for such an event to precede the deposition of dark matter-induced signals. Furthermore, the rate of these subsequent 1eh events appears to spike suddenly after the extremely high-energy event and then gradually decreases until the detector recovers. This behavior directly contradicts the Standard Halo Model, which assumes a uniform distribution of dark matter in the galactic halo.

Thus, neither the extremely high-energy event nor the subsequent 1eh events can be adequately explained by the dark matter hypothesis. Therefore, I conclude that the trigger rate spike phenomenon is highly unlikely to be caused by dark matter interactions. At the very least, it is not consistent with the dark matter models that the SuperCDMS HVeV program is designed to detect.

5.6.3 Hypothesis: Trapped Charges Delay Release

Although unconfirmed, a plausible explanation for the phenomenon is that it is caused by an extremely high-energy particle interacting with and damaging the silicon crystal surface. This impact could create a cluster of defects at the silicon surface, serving as traps for electrons and holes, while also generating a large number of electron-hole pairs. Many of these charges become captured at the surface defects.

The release of these trapped charges is governed by thermal effects. Since the HVeV detector operates at a temperature of 10 mK, the extremely low temperature significantly slows down the release rate. Additionally, the captured charges are continuously released and re-captured within the damaged region by the cluster of defects, forming a complex system. As a result, the rate of 1eh events detected by the detector approximately follows a $1/t$ decay pattern.

5.6.4 Explanation

All the small-energy events following the extremely high-energy event have an energy of 100 eV, making them 1eh events. This indicates that charges (electrons, holes, or electron-hole pairs) traveled through the entire crystal thickness and across the full 100 V applied voltage.

Initially, we focused on the possibility of external particles, such as photon, continuously injecting into the detector, as the events consistently exhibit an energy of 100 eV, which suggests real particle injection. Materials outside the detector could become excited and emit particles that continuously enter the detector crystal. At the beginning of the process, a large number of photons may be emitted simultaneously, resulting in the extremely high-energy event, as the sheer number of particles exceeds the detector's discrimination capability. Subsequently, the emission rate decreases, giving rise to what appears as a series of 1eh events.

However, as shown in Figure 5-8, the total energy of the subsequent 1eh events is not comparable to the energy of the initial extremely high-energy pulse. It is not straightforward to link the extremely high-energy pulse and the subsequent 1eh events to a single origin. Furthermore, the entire phenomenon lasts for approximately 10 hours, making it challenging to identify a mechanism capable of sustaining photon emission over such an extended period.

The XENON collaboration has reported a similar phenomenon in their dual-phase liquid xenon detectors: Single electrons correlated in time with a previous high-energy interaction have been observed out to times much longer than the maximum drift time of a free electron in the detector, and are sometimes known as "electron trains" [19]. The rate of the electron train also follows a $1/x$ decay pattern, with a typical timescale on the order of ms. The XENON collaboration trying to explains the electron trains as being caused by electrons trapped at the liquid-gas interface of the xenon detector or within impurities in the liquid phase.

The similarities between the XENON electron trains and the HVeV trigger rate spike lead me to consider the possibility that they share the same underlying physical mechanism. In the HVeV detector, I tend to think that electrons and holes are not simultaneously trapped within the bulk of the crystal. This is because the delayed events have energies exactly equal to 100 eV, implying that, under a bulk trapping scenario, one must assume that electron–hole pairs are trapped and subsequently released in perfect pairs, without undergoing recombination during the trapping period. This is an additional assumption that is relatively strong, even though I have not ruled out this possibility. However, a more natural explanation is that either electrons or holes are trapped at the detector surface and are gradually released by trapping centers over time. As these charge carriers are released, either electrons or holes drift across the entire crystal, depending on the direction of the applied electric field - and thereby acquire an energy of 100 eV.

The difference in timescales between the two effects can be naturally explained by the temperature difference. The XENON detector operates at approximately 100 K, while the HVeV detector operates at around 10 mK. The extremely low operating temperature of the HVeV detector significantly weakens thermal effects, causing electrons to take much longer to escape from the defects, the escaping rate $\mathrm{R} \propto \exp(-/\mathrm{T})$. Furthermore, the XENON detector likely experiences a higher background rate, which could obscure the tail of the electron trains, making them appear shorter in duration.

The paper [24] attributes the $1/x$ decay pattern to self-organized criticality (SOC), a characteristic feature of complex systems. If this is true, it raises an important question: where is the complex system in this context? I propose an explanation involving the initial extremely high-energy event. If this event is induced by a high-energy particle injecting into the detector and damaging the crystal surface, it could create clusters of defects or trapping states capable of holding many electrons. These clusters of trapping states could themselves form a complex system, potentially giving rise to the observed $1/x$ decay pattern. As electrons become trapped, they can be thermally released into the crystal. However, the escaping electrons may be re-captured by surrounding defects. The repeated capture and release of many electrons ultimately result in the characteristic $1/x$ decay pattern.

The DAMIC collaboration has studied the generation of crystal defects caused by high-energy particles with following conclusion: ”A preliminary spatial correlation analysis concludes that at least 80% of recoils with energies > 100 keVee produce measurable defects.” [21]. Such energy levels are attainable by background particles, making it plausible for these particles to damage the crystal surface.

If the entire phenomenon indeed occurs at the detector surface as predicted, the external particles responsible must have a limited penetration depth. The maximum penetration depth can be estimated based on the detector resolution. In HVeV Run 4, the detector resolution is 3.24 eV, and the applied voltage is 100 V across a 0.4 cm thickness crystal. This implies a maximum penetration depth of approximately (3.24 eV/100 eV) $\times$ 0.4 cm = 0.013 cm, beyond which the energy variation due to drift distance would be noticed by observing these events energy.

The minimum penetration depth can be inferred from the energy required to cause observable crystal damage. According to the DAMIC collaboration, particles with energies above 100 keVee can generate measurable structural damage in the crystal. Taking 100 keV as a conservative lower bound, the corresponding stopping range for different particle types can be used to estimate the minimum penetration depth.

Alpha particles are the most likely external particle candidate, as they can be produced in the vicinity of the detector. Furthermore, their typical energies correspond to penetration ranges that fall within the estimated limits discussed above.

5.6.5 Future Work

Even though it is reasonable to attribute the trigger rate spikes to high-energy particle injection, further work is still required to confirm this hypothesis. Here are some potential approaches for future investigation:

1. According to the assumption, temperature plays a crucial role in the long recovery time ($\tilde{1}$0 hours). Therefore, if researchers observe a trigger rate spike, they could test this hypothesis by increasing the detector's temperature from 10 mK to a higher value and then cooling it back to 10 mK. If the entire process can be completed in a relatively short time, such as 3 hours, it would be possible to distinguish the influence of temperature more clearly. This would allow researchers to determine whether the recovery time is indeed governed by thermal effects.

2. Proposing a simulation that accurately models the complex system could help reproduce the observed 1/x decay pattern. In a toy model, one could simulate a series of crystal defects and inject a population of electrons into the system. By observing the behavior of these electrons as they interact with and become trapped and released by the crystal defects, it

may be possible to recover the characteristic 1/x decay pattern. This approach could provide valuable insights into the mechanisms governing the phenomenon.

CHAPTER 6
HVeV RUN 4

HVeV Run 4 delineates the boundaries of sub-GeV dark matter limits, employing cutting-edge statistical tools and the latest detector designs.

6.1 Introduction

HVeV Run 4 is the fourth dark matter search conducted by the HVeV experiment. Motivated by successfully achieving the scientific goals of previous runs 1 to 3, HVeV Run 4 was undertaken with two specific science goals. These goals were assigned to two separate scientific runs, referred to as NEXUS Run 13 and NEXUS Run 14. NEXUS Run are HVeV-related experiments operated at Northwestern EXperimental Underground Site (NEXUS). NEXUS Run 13 aimed to release the latest dark matter limit results. NEXUS Run 14 sought to provide energy calibration for the Optimum Filter Estimator using an LED system, which can emit controllable standard energy photons.

In HVeV Run 4, a newly designed detector holder was introduced, from which PCBs were removed, leading to a significant reduction in background luminous events. Throughout the data analysis phase of HVeV Run 4, several new phenomena were studied, and newly developed statistical tools were utilized. HVeV Run 4 has successfully extended the dark matter limits into new territories.

6.2 Experiment Setup

The HVeV Run 4 experimental device was housed at the NEXUS, located at the Fermi National Accelerator Laboratory in Batavia, Illinois. A schematic diagram of NEXUS is shown in Figure 6-1. Situated 107 meters underground (equivalent to 300 meters water equivalent), this site provides an effective reduction in cosmic ray interference and also serves as a robust shield against radio frequency (RF) signals from human activities and other sources.

A clean room was constructed at NEXUS to minimize radiation from dust contamination. HVeV detectors were mounted inside a copper cavity, which serves both as a structural support for the detectors and as a moderate shielding layer. A CryoConcepts dilution refrigeration system 6-2 was employed to cool the detector crystals to 10.5 mK. During data collection, a metglas blanket

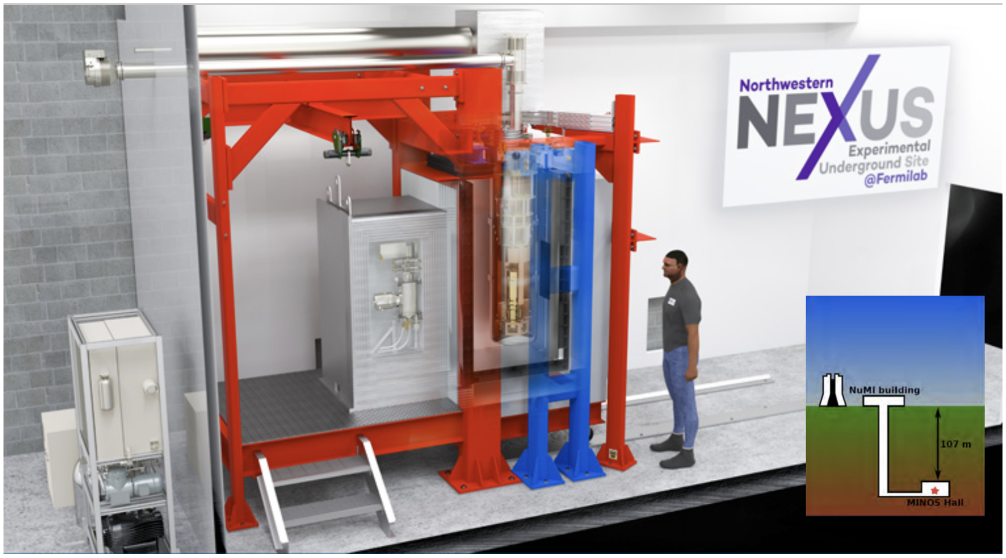

Figure 6-1. A schematic diagram of NEXUS. The dilution refrigerator is positioned in front of the person in the image and is partially enclosed by the blue support structure. The cubic box, located on the red support frame to the left of the dilution refrigerator, is the DD generator, which emits protons that produce 2.5 MeV neutrons. This generator was used for energy calibration in previous studies but was not applied in HVeV Run 4. The inset in the lower right corner illustrates the location of NEXUS, which is situated within the MINOS hall at Fermilab, approximately 107 meters underground.

was wrapped around the refrigerator to provide magnetic shielding, while lead bricks were placed around the refrigeration system to reduce gamma radiation from the surroundings.

The HVeV Run 4 utilized four detectors, referred to as NFC1, NFC2, NF-H, and NF-E, which were inherited from previous HVeV studies. Among these, only NFC1 data were used to set the final dark matter limits due to its lower noise conditions. HVeV Run 4 was conducted in 2022, with the dark matter limit-setting data based on NEXUS Run 13, collected between March 19 and March 30, 2022. Thirty percent of the data were used to develop and refine the data selection rules and algorithms. Once finalized, the remaining seventy percent of the blinded data were unblinded and used for setting the dark matter limits.

6.3 Live-Time Cuts

Live time cuts are applied directly in the time domain to remove abnormal events that are evidently inconsistent with dark matter models or are triggered by irrelevant sources. Four types

Figure 6-2. The dilution refrigerator system used in HVeV Run 4. The HVeV detectors are housed inside the refrigerator.

of live-time cuts are applied during the data analysis of HVeV Run 4: fridge temperature cut, TES baseline cut, trigger rate cut and coincidence cut.

6.3.1 Fridge Temperature Cut

The temperature of the mixing chamber was sampled every 40 seconds, allowing the temperature throughout HVeV Run 4 to be monitored continuously. The fridge temperature cut aims to remove data collected during periods when the mixing chamber temperature deviated from the set value. For HVeV Run 4, a threshold of 11.1 mK was applied. The algorithm identifies time periods where the temperature exceeds 11.1 mK and removes events occurring within these intervals. To further minimize the influence of temperature fluctuations, an extended time window is also excluded, covering additional periods before and after the threshold-exceeding intervals. This approach ensures that any residual effects from temperature changes are effectively reduced.

6.3.2 TES Baseline Cut

The raw current is continuously recorded and saved as a series of 0.5-second traces. The baseline refers to the value of the raw current when no events are occurring. The baseline cut ensures that the baseline current remains stable, as an unstable baseline can distort the shape of event pulses, leading to inaccuracies in the energy estimation of events.

The baseline cut first estimates the baseline value for each 0.5-second raw trace. If an event occurs within a trace, generating a pulse, the data surrounding the event is excluded. The remaining trace values are then averaged to determine the baseline value for that 0.5-second trace. The baseline values from all traces are subsequently analyzed using a Gaussian distribution to derive the mean and standard deviation. Traces with baseline values outside 3σ of the mean are rejected, ensuring that only events from traces that pass the baseline cut are included in the subsequent data analysis.

6.3.3 Trigger Rate Cut

As discussed in Section 5.6, the phenomenon of trigger rate spikes can introduce a significant number of 1eh events into the final dataset. Therefore, it is crucial to apply an effective event-cutting method to mitigate their impact. Initially, I attempted to model the event rate of 1eh events following a trigger rate spike. The event rate was first fitted using a double-exponential function, but exponential functions tend to decay faster than the actual observed rate. A $1/x$-shaped function was also considered. However, handling the divergence at the beginning proved challenging.

Ultimately, a 10-hour cut was implemented: once a trigger rate spike occurred, the subsequent 10 hours of data were excluded. After analyzing multiple instances of trigger rate spikes, it was determined that 10 hours is the optimal cut-off duration. Beyond this time frame, the contribution from trigger rate spikes becomes indistinguishable from the normal event rate.

6.3.4 Coincidence Cut

Based on the dark matter model under investigation, events triggered by dark matter particles are expected to be rare, resulting in a low predicted event rate. Consequently, events occurring consecutively within a short time frame are unlikely to be caused by dark matter and are therefore rejected.

In HVeV Run 4, data from the detector NFC1 was accepted as the primary science result, while the remaining three detectors served as veto detectors. Although veto detectors do not contribute directly to the science data, their readings are crucial for implementing coincidence cuts. The coincidence cut aims to reject two types of events:

1. Events that occur consecutively in time within a single detector.

2. Events that occur simultaneously in time across multiple detectors.

As a result, any consecutive events, whether within the same detector or across different detectors, are rejected. If an event satisfies either of the two conditions listed above, it is excluded from the final analysis.

6.3.5 Live-Time Cut Result

Most of the live time loss is due to the trigger rate cut, which alone accounts for 17.93% of the total live time loss, as trigger rate spikes tend to last for extended periods, even though the occurrence of such spikes is relatively rare. After applying all live time cuts, 19.46% of the total recorded time is lost, resulting in a remaining live time of 224.47 hours. The energy spectrum before and after live time cut is shown in Figure 6-4.

6.4 Energy Dependent χ^2 Cut

The χ^2 value is used to estimate the deviation of a pulse shape from the template. In SuperCDMS experiments, the χ^2 value is derived from its standard definition but includes optimizations to better align with experimental objectives. In principle, if the χ^2 value is equal to 1, the pulse perfectly matches the template. When the value of χ^2 is greater than 1, it indicates that the pulse shape begins to deviate from the template, with larger values of χ^2 corresponding to greater deviations.

In the experiment, due to the presence of random noise, every pulse shape deviates slightly from the template. Most pulses have χ^2 values distributed randomly around a mean slightly greater than 1, and this distribution can typically be modeled by a Gaussian function. However, beyond the influence of noise, significant deviations can occur under certain conditions, such as unstable baselines or overlapping pulses occurring in quick succession. These scenarios can cause substantial distortion in the pulse shape, resulting in χ^2 values as high as 10, 100, or even larger.

Figure 6-3 (A) shows the χ^2 values and energy of events recorded by detector NFC1 under a Cs-137 source. The Cs-137 source significantly increases the event rate, providing sufficient data to analyze their statistical properties. In the plot, data points clustered around $\chi^2 = 1$ represent the first class of events, as described earlier. These events are considered to have good pulse shapes influenced primarily by noise, and the χ^2 cut parameters are derived from this data set. In contrast, the remaining data points, particularly those with significantly larger χ^2 values (e.g., the cluster in the upper left of the plot), deviate strongly from the pulse template. These events are excluded from the calculation of χ^2 parameters due to their poor fit to the template thus is considering as non-event pulses.

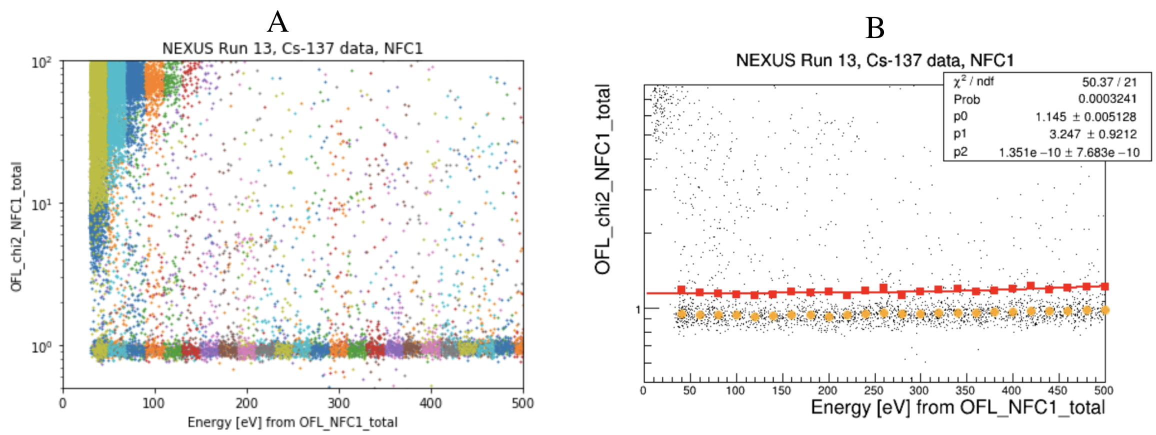

Figure 6-3. χ^2 vs. Energy Distribution for Data Recorded in the Presence of a Cs-137 Source. (A) The distribution of χ^2 values for all recorded events, ranging from approximately 0.5 to 100. Data points are grouped in 20 eV energy bins. The majority of events cluster around $\chi^2 = 1$, and these are analyzed to determine the appropriate χ^2 cut. (B) A zoomed-in view of the χ^2 values, focusing on the range from 0.5 to 10. Orange points represent the mean χ^2 value for each 20 eV energy bin, obtained through Gaussian fitting. Red points indicate the threshold at three standard deviations from the mean, and the red curve represents the final energy-dependent χ^2 cut applied to the data.

As shown in Figure 6-3 (B), the cluster of data centered around $\chi^2 = 1$ exhibits non-linearity within the energy range, indicating that data should be analyzed with consideration of their energy dependence. These data is collected and divided into 20 eV intervals, ranging from 30 eV to 510 eV. For each subgroup, a Gaussian fit is applied to the distribution of χ^2 values to determine the mean (μ) and standard deviation (σ). In Figure 6-3, the orange square points represent the mean χ^2 value for each 20-eV energy range, while the red square points indicate the χ^2 value corresponding to $\mu + 3 \cdot \sigma$. The $\mu + 3 \cdot \sigma$ values for all 20 eV intervals are then fitted using the function $\chi^2 = p_0 + p_1 \cdot E^{p_2}$. Any data points with χ^2 values exceeding this function are rejected. The energy spectrum of the data after applying the live time cuts and χ^2 cut is shown in green in Figure 6-4.

6.5 Limit Setting

After applying live time cuts and data quality cuts, the remaining data points are passed to the final limit-setting procedure. In HVeV Run 4, the number of events within the first four electron-hole pair peaks is counted and analyzed. The profile likelihood method [13] is used to set the dark matter limits, replacing the Poisson counting method used in HVeV Run 3. This approach accounts for the impact of nuisance parameters such as detector resolution, charge trapping fraction, impact ionization fraction, etc. ensuring a more robust analysis.

6.5.1 Likelihood Functions

The likelihood function $\mathcal{L}$ quantifies how well the experimental data align with a given statistical model. It represents the possibility of observing the data under specific model parameters. By maximizing the value of the likelihood function, one can determine the set of model parameters that best explain the observed data.

In a typical dark matter direct detection experiment, the likelihood function consists of three different terms:

1. Event Number Term 6-1: this term accounts for the statistical variation in the observed event counts, modeled as a Poisson process.

2. Discrimination Term 6-2: this term incorporates the ability of distinguishing signal events from background events based on the probability density function of signal and background.

3. Constraints Term 6-3: this term incorporates prior constraints on nuisance parameters, ensuring their variations are properly accounted for in the analysis.

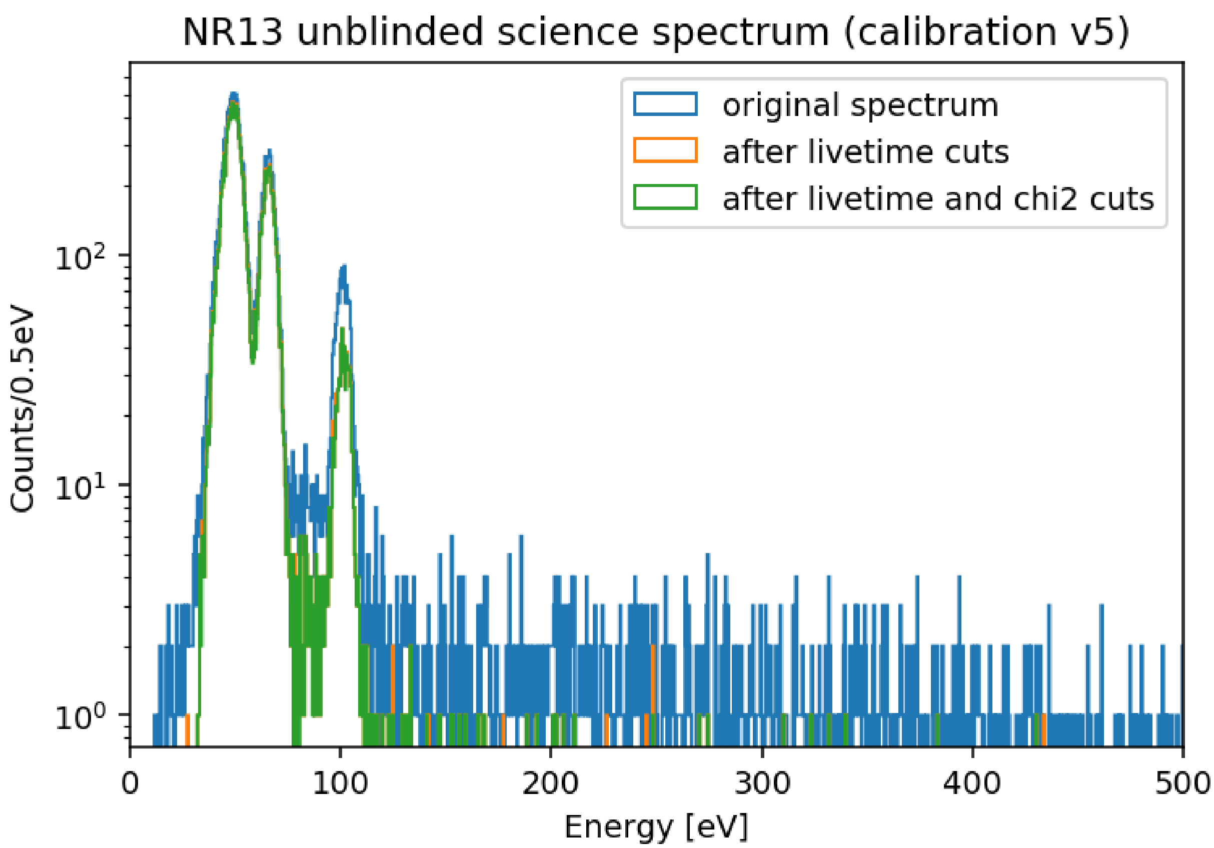

Figure 6-4. A comparison of the event energy spectra from HVeV Run 4 unblinded science data at different stages of data selection: before any cuts, after applying the livetime cuts, and after applying both the livetime cuts and the χ^2 cut. Credit: SuperCDMS collaboration.

$$\mathcal{L}_{\text{Poisson}} = \left[\nu_\chi + \sum_b \nu_b\right]^N \times \frac{\exp\left[-\left(\nu_\chi + \sum_b \nu_b\right)\right]}{N!} \tag{6-1}$$

In event number term, ν_χ represents the expected number of events caused by dark matter, which is predicted by the signal mode. While $\sum_b \nu_b$ denotes the total expected number of events from all background sources. N is the number of events observed in the experiment. The number of events due to dark matter in a unit of time is expected to follow a Poisson distribution, and therefore, the likelihood function $\mathcal{L}_{\text{Poisson}}$ is modeled as a Poisson distribution.

$$\mathcal{L}_{\chi,b} = \prod_{i=1}^{N} \left[H_\chi(E_i) + \sum_b H_b(E_i)\right] \tag{6-2}$$

In the discrimination term, E_i represents the measured energy in the i^{th} bin, $H_\chi(E)$ is the probability density function of the signal, it can be predicted by the signal model 4-15. Term $\sum_b H_b(E_i)$ is the sum of the probability density functions from all background sources. The likelihood function$\mathcal{L}_{\chi,b}$ incorporates contributions from all bins by multiplying the results across all bins.

$$\mathcal{L}_{constr.} = \prod_k \frac{1}{\sqrt{2\pi\sigma_k^2}} e^{-(\theta_k - m_k)^2/2\sigma_k^2} \tag{6-3}$$

Constraints on nuisance parameters are included in the constraints term. Each nuisance parameter, which may depend on experimental conditions, is assumed to fluctuate around its true value and is modeled as a Gaussian distribution. Here, θ_k represents the allocated value of the k^{th} nuisance parameter. This parameter can appear in both the event number term and the discrimination term, making the three likelihood functions interdependent. The parameters m_k is the true value of the k^{th} nuisance parameter, and σ_k is the standard deviation of the k^{th} nuisance parameter, they are determined through subsidiary experiments.

In HVeV Run 4, a signal-only profile likelihood method is adopted, thus all the events are assumed to be come from dark matter interaction. Under signal-only assumption, parameters that relate to backgrounds are assumed to be zero. Thus, the final total likelihood function is given in Equation 6-4.

$$\mathcal{L}_{tot}(\mu|\theta_1, \theta_2, ..., \theta_k) = \nu_\chi^N \times \frac{\exp(-\nu_\chi)}{N!} \times \prod_{i=1}^{N} H_\chi(E_i) \times \prod_k \frac{1}{\sqrt{2\pi\sigma_k^2}} e^{-(\theta_k - m_k)^2/2\sigma_k^2} \tag{6-4}$$

Here, μ represents the parameter of interest, which varies depending on the dark matter interaction model: it corresponds to the cross section σ_e for the dark matter-electron scattering model, the kinetic mixing parameter ε for the dark photon absorption model, and the axio-electric coupling constant g_{ae} for the axion-like particle absorption model. The parameters $\theta_1, \theta_2, ..., \theta_k$ are nuisance parameters. The expected event numbers, ν_χ, can be calculated as:

$$\nu_\chi = Exposure \cdot \int_a^b R_{tot} \cdot H(E) \cdot \epsilon(E) dE \tag{6-5}$$

In the HVeV experiment, $Exposure$ is in unit of $gram \cdot day$, it is defined as the product of the detector's target mass and the live time, which represents the total amount of target material exposed to potential interactions over a given time period. $R_{tot} \cdot H(E)$ is the differential rate, as described in Equation 4-16 of chapter signal model. $\epsilon(E)$ is the data quality cut efficiency, quantifies the fraction of signal events at energy E that pass all applied selection cuts.

6.5.2 Profile Likelihood Method

The profile likelihood method [13] is applied to set dark matter limits, and the profile likelihood is defined as:

$$\lambda(\mu) = \frac{\mathcal{L}_{tot}(\mu, \hat{\hat{\theta}}_1, \hat{\hat{\theta}}_2, ..., \hat{\hat{\theta}}_k)}{\mathcal{L}_{tot}(\hat{\mu}, \hat{\theta}_1, \hat{\theta}_2, ..., \hat{\theta}_k)} \tag{6-6}$$

Here, the likelihood function $\mathcal{L}_{tot}$, defined in Equation 6-4, is the function of the parameter of interest μ and the nuisance parameters $\theta_1, \theta_2, ..., \theta_k$. The terms $\hat{\hat{\theta}}_1, \hat{\hat{\theta}}_2, ..., \hat{\hat{\theta}}_k$ represent the values of the nuisance parameters that maximize $\mathcal{L}_{tot}$ for a fixed value of μ. In contrast,

$\hat{\mu}, \hat{\theta}_1, \hat{\theta}_2, ..., \hat{\theta}_k$ denote the values of $\mu, \theta_1, \theta_2, ..., \theta_k$ that globally maximize $\mathcal{L}_{tot}$ without any constraints on μ. Consequently, once the form of $\mathcal{L}_{tot}$ is defined, the values of $\hat{\mu}, \hat{\theta}_1, \hat{\theta}_2, ..., \hat{\theta}_k$ and $\mathcal{L}_{tot}(\hat{\mu}, \hat{\theta}_1, \hat{\theta}_2, ..., \hat{\theta}_k)$ remain fixed. However, the values of $\hat{\hat{\theta}}_1, \hat{\hat{\theta}}_2, ..., \hat{\hat{\theta}}_k$ and $L_{tot}(\mu, \hat{\hat{\theta}}_1, \hat{\hat{\theta}}_2, ..., \hat{\hat{\theta}}_k)$ vary as μ changes.

In HVeV Run 4, the signal-only assumption is adopted, and the limit setting is based on the q_u statistic [13], where the parameter of interest μ is constrained to have an upper limit. The q_u statistic is defined as:

$$q_\mu = \begin{cases} -2 \cdot ln\lambda(\mu), & \hat{\mu} < \mu, \\ 0, & \hat{\mu} > \mu, \end{cases} \tag{6-7}$$

Here, μ represents the parameter of interest that we aim to investigate, while $\hat{\mu}$ denotes the global maximum likelihood estimator, as used in Equation 6-6. In HVeV Run 4, the dark matter parameter is constrained at a 90% confidence level, which means that the upper limit on μ is set such that the probability of obtaining a test statistic as extreme as the observed one, assuming μ is true, is 10%. The p-value is calculated as:

$$p = \int_{q_{\mu,\text{Exp.}}}^{\infty} f(q_\mu|\mu)\, dq_\mu \tag{6-8}$$

where $q_{\mu,\text{Exp.}}$ represents the value of q_μ derived from the measured experimental data, and $f(q_\mu|\mu)$ denotes the probability density function of q_μ for a given hypothesis of μ. The specific form of $f(q_\mu|\mu)$ can be obtained using either the Wald approximation or Monte Carlo simulations.

To set dark matter limits, a range of dark matter masses must be considered, requiring the selection of representative mass points across the range. For each mass hypothesis, the largest value of μ for which $p = 0.1$ is taken as the upper limit at 90% confidence level. This requires constructing $f(q_\mu|\mu)$, which depends on the chosen method.

To derive $f(q_\mu|\mu)$, in HVeV Run 4, the Wald approximation is applied in the region of the first electron-hole pair peak, as the number of data points is sufficient to satisfy the conditions for its validity. However, for the second, third, and fourth electron-hole pair peak regions, the number of events can be very small, making the Wald approximation less reliable. Therefore, Monte Carlo simulation is employed instead.

When using Monte Carlo simulations, nuisance parameters related to experimental conditions are randomly sampled from their prior distributions, which are characterized by their mean m_k and standard deviation σ_k. The probability density function of the signal, $H(E)$, is also randomly generated. These components are then used to simulate ”fake experiments” by generating fake events, each assigned an energy based on the model.

For a given value of μ, a large number of fake experiments are generated to build a statistically robust dataset. This dataset is used to construct the probability density function of q_μ for the given μ. By identifying the value of μ that satisfies $p = 0.1$, the corresponding upper limit on the signal parameter is determined.

6.6 Results

The HVeV Run 4 focuses on exploring three dark matter interaction models:

1. Dark matter-electron scattering (DMe) model, with two different form factors - 1 and $\frac{1}{q^2}$.

2. Dark photon absorption (DPA) model.

3. Axion-like particles (ALP) absorption model.

The Figure 6-5 present the dark matter limits derived from the HVeV Run 4 experiments. Compared to HVeV Run 3, the latest limits significantly extend into lower parameter space, primarily due to the successful removal of PCB luminescence events. Additionally, the updated dark matter limits are highly competitive when compared to other existing constraints.

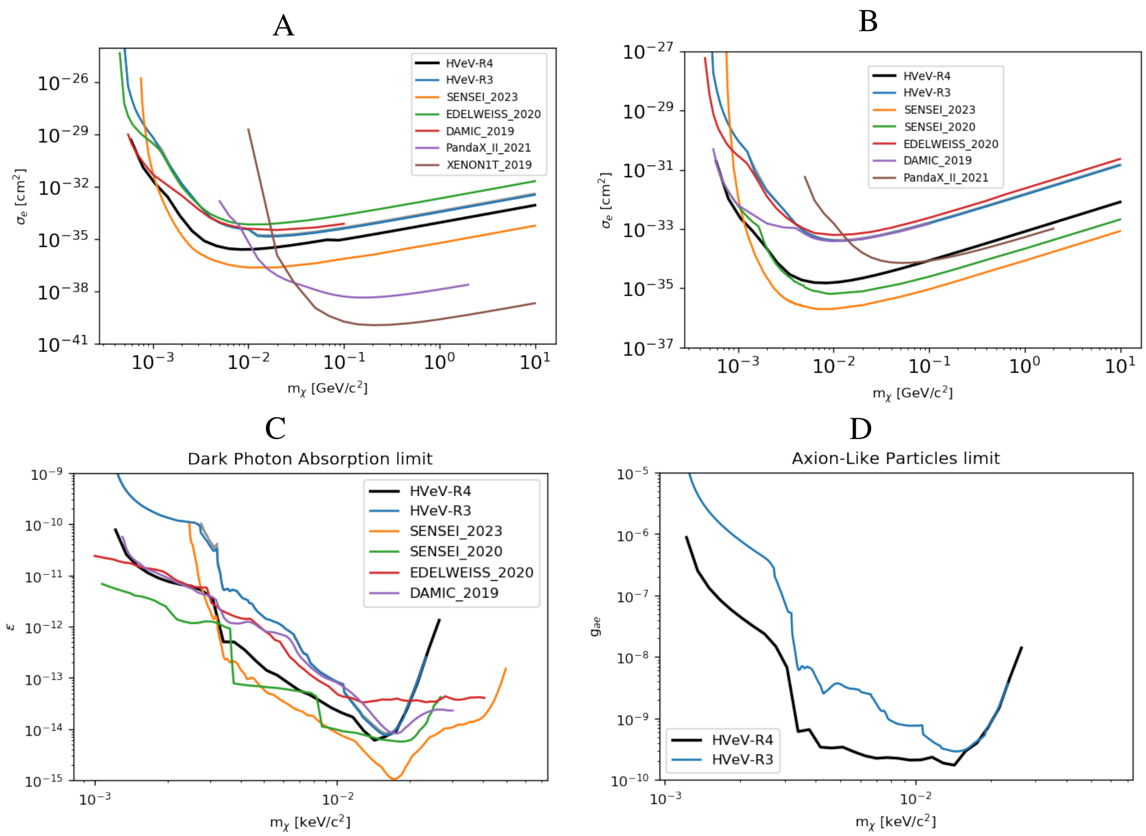

Figure 6-5. Latest dark matter exclusion limits from HVeV Run 4, compared with results from HVeV Run 3 and other experiments. (A) Exclusion limits on the dark matter-electron scattering cross section with a form factor of 1. (B) Exclusion limits on the dark matter-electron scattering cross section with a form factor proportional to $1/q^2$. (C) Exclusion limits on the kinetic mixing parameter ϵ for the dark photon absorption model. (D) Exclusion limits on the effective axion-electron coupling g_{ae} for the axion-like particle model. Credit: SuperCDMS collaboration.

The analysis process described in this chapter is an integral part of the overall limit-setting procedure. For HVeV Run 4, the team introduced numerous new analysis techniques and applied more advanced statistical methods to the data. However, due to space constraints, it is not possible to detail all of them here.

LIST OF REFERENCES

[1] Prakruth Adari et al., *First Direct-Detection Results on Sub-GeV Dark Matter Using the SENSEI Detector at SNOLAB*, Phys. Rev. Lett. **134** (2025), no. 1, 011804.

[2] P. Adhikari et al., *The liquid-argon scintillation pulseshape in DEAP-3600*, Eur. Phys. J. C **80** (2020), no. 4, 303.

[3] M. F. Albakry et al., *Investigating the sources of low-energy events in a SuperCDMS-HVeV detector*, Phys. Rev. D **105** (2022), no. 11, 112006.

[4] Albakry, M. F. et al., *Light dark matter constraints from SuperCDMS HVeV detectors operated underground with an anticoincidence event selection*, Phys. Rev. D **111** (2025), no. 1, 012006.

[5] J. Angle et al., *A search for light dark matter in XENON10 data*, Phys. Rev. Lett. **107** (2011), 051301, [Erratum: Phys.Rev.Lett. 110, 249901 (2013)].

[6] Elena Aprile, *The XENON program for dark matter direct detection*, Nucl. Phys. B **1003** (2024), 116463.

[7] Siska De Baerdemaeker, *Method-Driven Experiments and the Search for Dark Matter*, Phil. Sci. **88** (2021), no. 1, 124–144.

[8] Marco Battaglieri et al., *US Cosmic Visions: New Ideas in Dark Matter 2017: Community Report*, U.S. Cosmic Visions: New Ideas in Dark Matter, 7 2017.

[9] R. Bernabei et al., *First results from DAMA/LIBRA and the combined results with DAMA/NaI*, Eur. Phys. J. C **56** (2008), 333–355.

[10] Gianfranco Bertone and Dan Hooper, *History of dark matter*, Rev. Mod. Phys. **90** (2018), no. 4, 045002.

[11] Michael A. Bowles, *Minimizing Backgrounds for the SuperCDMS SNOLAB Dark-Matter Experiment*, Ph.D. thesis, South Dakota School of Mines and Technology, 2019.

[12] Susana Cebrián, *Review on dark matter searches*, J. Phys. Conf. Ser. **2502** (2023), no. 1, 012004.

[13] Glen Cowan, Kyle Cranmer, Eilam Gross, and Ofer Vitells, *Asymptotic formulae for likelihood-based tests of new physics*, Eur. Phys. J. C **71** (2011), 1554, [Erratum: Eur.Phys.J.C 73, 2501 (2013)].

[14] Rouven Essig, Marivi Fernandez-Serra, Jeremy Mardon, Adrian Soto, Tomer Volansky, and Tien-Tien Yu, *Direct Detection of sub-GeV Dark Matter with Semiconductor Targets*, JHEP **05** (2016), 046.

[15] Rouven Essig, Jeremy Mardon, and Tomer Volansky, *Direct Detection of Sub-GeV Dark Matter*, Phys. Rev. D **85** (2012), 076007.

[16] Marco Fabbrichesi, Emidio Gabrielli, and Gaia Lanfranchi, *The Dark Photon*, (2020).

[17] Katherine Freese, Mariangela Lisanti, and Christopher Savage, *Colloquium: Annual modulation of dark matter*, Rev. Mod. Phys. **85** (2013), 1561–1581.

[18] Yonit Hochberg, Tongyan Lin, and Kathryn M. Zurek, *Absorption of light dark matter in semiconductors*, Phys. Rev. D **95** (2017), no. 2, 023013.

[19] Abigail Kopec, Amanda L. Baxter, Michael Clark, Rafael F. Lang, Shengchao Li, Juehang Qin, and Riya Singh, *Correlated single- and few-electron backgrounds milliseconds after interactions in dual-phase liquid xenon time projection chambers*, JINST **16** (2021), no. 07, P07014.

[20] Noah Alexander Kurinsky, *The Low-Mass Limit: Dark Matter Detectors with eV-Scale Energy Resolution*, Ph.D. thesis, Stanford U., Phys. Dept., 2018.

[21] Steven J. Lee, *Analysis of radiation damage in silicon charge-coupled devices used for dark matter searches*, SciPost Phys. Proc. **12** (2023), 030.

[22] S. Navas et al., *Review of particle physics*, Phys. Rev. D **110** (2024), no. 3, 030001.

[23] Jack Nelson, *Backgrounds and shielding for supercdms snolab*, Presented at the 2021 Meeting of the Division of Particles and Fields of the American Physical Society (DPF21), July 2021.

[24] Sergey Pereverzev, *Dark matter searches and energy accumulation and release in materials*, SciPost Phys. Proc. **12** (2023), 009.

[25] F. Ponce et al., *Modeling of Impact Ionization and Charge Trapping in SuperCDMS HVeV Detectors*, J. Low. Temp. Phys. **199** (2020), no. 3-4, 598–605.

[26] Stefano Profumo, Leonardo Giani, and Oliver F. Piattella, *An Introduction to Particle Dark Matter*, Universe **5** (2019), no. 10, 213.

[27] Viktor Pěč, Vitaly A. Kudryavtsev, Henrique M. Araújo, and Timothy J. Sumner, *Muon-induced background in a next-generation dark matter experiment based on liquid xenon*, Eur. Phys. J. C **84** (2024), no. 5, 481.

[28] K. Ramanathan and N. Kurinsky, *Ionization yield in silicon for eV-scale electron-recoil processes*, Phys. Rev. D **102** (2020), no. 6, 063026.

[29] Tarek Saab, *A survey of dark matter direct detection searches and techniques at the beginning of the 21st century*, Mod. Phys. Lett. A **23** (2008), 457–475.

[30] D. Speller, *Dark matter direct detection with SuperCDMS Soudan*, J. Phys. Conf. Ser. **606** (2015), no. 1, 012003.

[31] Javier Tiffenberg, Miguel Sofo-Haro, Alex Drlica-Wagner, Rouven Essig, Yann Guardincerri, Steve Holland, Tomer Volansky, and Tien-Tien Yu, *Single-electron and single-photon sensitivity with a silicon Skipper CCD*, Phys. Rev. Lett. **119** (2017), no. 13, 131802.

[32] V. Tomasello, M. Robinson, and V. A. Kudryavtsev, *Radioactive background in a cryogenic dark matter experiment*, Astropart. Phys. **34** (2010), 70–79.

[33] T. S. van Albada, John N. Bahcall, K. Begeman, and R. Sancisi, *The Distribution of Dark Matter in the Spiral Galaxy NGC-3198*, Astrophys. J. **295** (1985), 305–313.

[34] Simon Viel, *Latest results from the DEAP-3600 experiment at SNOLAB*, PoS **TAUP2023** (2024), 075.

[35] M. J. Wilson et al., *Improved modeling of detector response effects in phonon-based crystal detectors used for dark matter searches*, Phys. Rev. D **109** (2024), no. 11, 112018.

[36] R. L. Workman et al., *Review of Particle Physics*, PTEP **2022** (2022), 083C01.

BIOGRAPHICAL SKETCH

Huanbo's interest in physics originates from his first class in junior high school, in which his physics teacher did some interesting small experiments that totally went against common sense, like magic. Since then, Huanbo started diving into the physics world. As the study went deeper, the regulations of the world attracted him further. He was amazed that a simple rule could explain the complex world.

As Huanbo entered senior high school, he kept working hard in physics class, while also starting to consider the possibility of going further in this field in the future. He wanted to choose physics as his undergraduate major; however, his family didn't agree with his choice, considering the difficulty of finding a job in the future. Huanbo was young and hadn't realized the importance of making free choices for his own life. He eventually enrolled in electrical engineering as his major.

After Huanbo spent four years studying electrical engineering, he realized he still liked physics. After some struggling, he made a far-reaching decision: enter graduate school and transfer his major to physics. With his father's support, he then entered the Illinois Institute of Technology in Chicago in the year of 2017.

Huanbo received his master's degree at Illinois Institute of Technology. The time he studied in Chicago was the most substantial period over the many years. He studied really hard to learn the physics classes that he should have learned. He also joined an experimental group led by Prof. Segre.

In 2019, Huanbo entered the University of Florida for his doctoral degree. He originally intended to join a theoretical group to study particle physics. Unluckily, he didn't find a position in the theoretical group. However, Huanbo still wanted to work in the field of particle physics, and he was lucky that Prof. Saab offered him a chance in the experimental group to do dark matter experiments. Huanbo then started to progress in this research field. At the beginning, everything was new and interesting for Huanbo, and he studied hard. However, he couldn't adapt to life in Gainesville, and because of the COVID pandemic, Huanbo couldn't find connection between people — boredom and loneliness were the theme of this period. Furthermore, the real research was not as he imagined. He lost his goal and interest in research, and that was a hard period of his life. After a long time of hesitation and struggling, he started to reconcile with himself. He began to reexamine everything he had thought and done. He finally recovered from the lifeless condition.

Time flew, and it quickly came to 2025. Huanbo finished all his studies at the University of Florida, successfully passed his Ph.D. defense in May, and received his Doctor of Philosophy degree from the University of Florida in the spring of 2025.